

# CHROMOSPHERIC MAGNETIC FIELD: A COMPARISON OF HE I 10830 Å OBSERVATIONS WITH NONLINEAR FORCE-FREE FIELD EXTRAPOLATION

YUSUKE KAWABATA,<sup>1</sup> ANDRÉS ASENSIO RAMOS,<sup>2,3</sup> SATOSHI INOUE,<sup>4</sup> AND TOSHIFUMI SHIMIZU<sup>5,6</sup>

<sup>1</sup>*National Astronomical Observatory of Japan, 2-21-1 Osawa, Mitaka, Tokyo 181-8588, Japan*

<sup>2</sup>*Instituto de Astrofísica de Canarias, C/Vía Láctea s/n, 38205, La Laguna, Tenerife, Spain*

<sup>3</sup>*Departamento de Astrofísica, Universidad de La Laguna, 38206, La Laguna, Tenerife, Spain*

<sup>4</sup>*Institute for Space-Earth Environmental Research, Nagoya University, Furo-cho, Chikusa-ku, Nagoya, 464-8601, Japan*

<sup>5</sup>*Institute of Space and Astronautical Science, Japan Aerospace Exploration Agency, 3-1-1 Yoshinodai, Chuo, Sagami-hara, Kanagawa 252-5210, Japan*

<sup>6</sup>*Department of Earth and Planetary Science, The University of Tokyo, 7-3-1 Hongo, Bunkyo-ku, Tokyo 113-0033, Japan*

## ABSTRACT

The nonlinear force-free field (NLFFF) modeling has been extensively used to infer the three-dimensional (3D) magnetic field in the solar corona. One of the assumptions in the NLFFF extrapolation is that the plasma beta is low, but this condition is considered to be incorrect in the photosphere. We examine direct measurements of the chromospheric magnetic field in two active regions through spectropolarimetric observations at He I 10830 Å, which are compared with the potential fields and NLFFFs extrapolated from the photosphere. The comparisons allow quantitative estimation of the uncertainty in the NLFFF extrapolation from the photosphere. Our analysis shows that observed chromospheric magnetic field may have larger non-potentiality compared to the photospheric magnetic field. Moreover, the large non-potentiality in the chromospheric height may not be reproduced by the NLFFF extrapolation from the photospheric magnetic field. The magnitude of the underestimation of the non-potentiality at chromospheric heights may reach 30-40 degree in shear signed angle in some locations. This deviation may be caused by the non-force-

freeness in the photosphere. Our study suggests the importance of the inclusion of measured chromospheric magnetic fields in the NLFFF modeling for the improvement of the coronal extrapolation.

*Keywords:* Sun: coronal mass ejections — Sun: flares — Sun: X-rays, gamma rays

## 1. INTRODUCTION

Many energetic events, such as solar flares and coronal mass ejections (CMEs), are caused by the release of the magnetic field energy stored in the solar corona. Obtaining the magnetic field information in the solar atmosphere is crucial task to understand the mechanisms of such dynamic events. The solar magnetic field is routinely measured via spectropolarimetric observations in the photosphere and chromosphere (de la Cruz Rodríguez & van Noort 2017). On the other hand, the coronal magnetic field is difficult to obtain due to the lower brightness of the coronal lines.

The force-free field modeling is one of the alternative methods to infer the three-dimensional (3D) magnetic field in the solar corona. The main concept of the force-free field modeling is to extrapolate the magnetic field lines from the spatial map of the magnetic field in the photosphere based on two assumptions; low plasma beta and mechanical equilibrium in the solar corona (Wiegelmann & Sakurai 2012). The two assumptions lead to the condition that the Lorentz force vanishes in the solar corona, i.e., the magnetic tension and the magnetic pressure are balanced. That is,

$$\mathbf{j} \times \mathbf{B} = 0, \quad (1)$$

where  $\mathbf{j}$  is the current density, and  $\mathbf{B}$  is the magnetic field. Eqn. (1) can be rewritten by using Ampère's law  $\nabla \times \mathbf{B} = 4\pi\mathbf{j}/c$ , so that

$$\nabla \times \mathbf{B} = \alpha\mathbf{B}, \quad (2)$$

where  $\alpha$  is the force-free parameter. When  $\alpha$  has a spatial dependence, the magnetic field distribution is known as *nonlinear force-free field* (NLFFF).

One of the most controversial problems in NLFFF extrapolation is the assumption of force-freeness in the photosphere. From the model of Gary (2001), the plasma beta in plage regions in the photosphere is of order of  $10^2$ , while the magnetic field at the center of sunspots is almost force-free. There are some previous studies to investigate the force-freeness in active regions in the photosphere based on the force-free condition derived by Low (1985). The Lorentz force can be written as the divergence of the Maxwell stress tensor,

$$M_{ij} = -\frac{B^2}{8\pi}\delta_{ij} + \frac{B_i B_j}{4\pi}. \quad (3)$$

Assuming that the strength of magnetic field vanishes at very large heights, three cartesian components of the volume-integrated Lorentz force can be approximately written with the following surface integrals:

$$F_x = \frac{1}{4\pi} \int B_x B_z dx dy, \quad (4)$$

$$F_y = \frac{1}{4\pi} \int B_y B_z dx dy, \quad (5)$$

$$F_z = \frac{1}{8\pi} \int (B_z^2 - B_x^2 - B_y^2) dx dy. \quad (6)$$

According to [Low \(1985\)](#), the magnetic field is force-free if the three components of the net Lorentz force are smaller than the integrated magnetic pressure force:

$$F_p = \frac{1}{8\pi} \int (B_x^2 + B_y^2 + B_z^2) dx dy. \quad (7)$$

[Metcalf et al. \(1995\)](#) investigated the force-freeness in the photosphere and the chromosphere using observations of the Na I 5896 Å line. They showed that while  $|F_z|/F_p \sim 0.4$  in the photosphere,  $|F_z|/F_p$  becomes 0.1 roughly 400 km above the photosphere and concluded that the photosphere is not force-free while the chromosphere is indeed force-free. [Moon et al. \(2002\)](#) analyzed 12 magnetograms obtained from the Fe I pair of lines at 6301.5 and 6302.5 Å and showed that the value of  $|F_z|/F_p$  ranges from 0.06 to 0.32 with a median value of 0.13. This result implies that the photospheric magnetic field is not far from the force-free state. On the other hand, [Liu et al. \(2013\)](#) performed a statistical study of the force-freeness using 925 magnetograms and found that only 25% of the active regions satisfy  $|F_z|/F_p < 0.1$ . We note that the conditions described by [Low \(1985\)](#) are not sufficient for force-freeness.

The validity of the NLFFF modeling has been checked by X-ray and/or extreme ultraviolet (EUV) imaging observations. Imaging observations have the disadvantage that quantitative information about the magnetic field strength can not be obtained. Moreover, X-ray and/or EUV observations suffer from projection effects and are sensitive to the presence of multiple loops along the line of sight. Therefore, how the non-force-freeness in the photosphere can affect the 3D configuration of the magnetic field in the NLFFF modeling is still unclear.

To reveal the NLFFF uncertainty in the upper atmosphere, we make use of spectropolarimetric observations with chromospheric spectral lines for two active regions and derive the chromospheric magnetic

field. The derived chromospheric magnetic field is compared with the potential as well as NLFFF extrapolations from the photospheric magnetic field. Using the magnetic field in the chromosphere, being a layer between the photosphere and the corona, can help better understand the phenomena occurring in active regions. First, the magnetic field in the chromosphere will play an important role in improving extrapolation methods. Although the force-freeness of the photospheric magnetic field in active regions is controversial, the chromospheric magnetic field is thought to be sufficiently force-free (Metcalf et al. 1995; Gary 2001). Therefore, using the chromospheric magnetic field as the bottom boundary can improve the NLFFF modeling of the coronal magnetic field. Second, we can quantitatively compare the NLFFF modeling from both the photosphere and chromosphere and understand the effect of the non-force-freeness. Third, the chromospheric magnetic field measurements will help us to understand the onset mechanisms of solar flares. Recent works suggest that a magnetic reconnection in chromospheric layers is a suitable mechanism for the onset of solar flares (Kusano et al. 2012; Bamba et al. 2013; Wang et al. 2017).

Accurate measurements of the chromospheric magnetic field are challenging. The magnetic field in the chromosphere has been qualitatively and quantitatively measured with ground-based telescopes using the Ca II H & K lines (3934 and 3968 Å), H $\alpha$  (6563 Å), Ca II infrared lines (8949, 8542, and 8662 Å), and He I lines at 5876 and 10830 Å (see the review of de la Cruz Rodríguez & van Noort 2017). In the solar atmosphere, the Zeeman effect and the Hanle effect are the primary mechanisms to produce polarimetric signals in these spectral lines in the presence of the magnetic field. The Hanle effect modifies polarization signals which are produced by the scattering polarization when the magnetic field is inclined with respect to the symmetry axis of the radiation field (e.g., Trujillo Bueno 2001). Compared to the Zeeman effect, the Hanle effect is sensitive to weaker fields, typically in the range between 1 and 100 G for selected solar spectral lines. One of the difficulties to infer the magnetic field in the chromosphere from spectropolarimetric observations is the necessity of the complex atmospheric model. For example, the Ca II K and H $\alpha$  lines need to be modeled in non-local thermodynamic equilibrium (NLTE) (Vernazza et al. 1981). On the contrary, He I 10830 Å which results from the transition between the terms  $2s^3S$  and  $2p^3P$  of the triplet system of He I is simpler to model. The only feasible way to populate the lower term of the multiplet is via EUV radiation from the

corona. Therefore, the formation layer of He I 10830 Å is thinner compared to other chromospheric lines, which makes it possible to interpret the line with a simple constant slab model.

[Solanki et al. \(2003\)](#) determined the chromospheric vector magnetic field in small emerging active regions through the inversion of the spectropolarimetric data at He I 10830 Å. They revealed the existence of a tangential discontinuity of the magnetic field direction, which is the observational signature of an electric current sheet. The magnetic field vector at other chromospheric features has also been studied; active region filaments ([Xu et al. 2012](#)), superpenumbral fine structures ([Schad et al. 2013, 2015](#)), and sunspots ([Joshi et al. 2017](#)). The usage of force-free magnetic field boundary conditions for the NLFFF modeling has also been investigated. One of the methods is the preprocessing method, with which we can obtain magnetic fields similar to those in the chromosphere from photospheric observations. This preprocessing method was firstly proposed by [Wiegmann et al. \(2006\)](#), which consists of minimizing the total force and torque on the bottom boundary. [Yamamoto & Kusano \(2012\)](#) developed a new preprocessing method with chromospheric magnetic field. They improved the method by adding a new term concerning chromospheric longitudinal fields. They found that some preprocessed fields display the smallest force- and torque-freeness. [Yelles Chaouche et al. \(2012\)](#) investigated the three-dimensional structure of an active region filament by using NLFFF extrapolations based on simultaneous observations at photospheric (Si I 10827 Å) and chromospheric (He I 10830 Å) heights. The extrapolations yield a twisted flux rope whose axis is located at about 1.4 Mm above the solar surface.

In this work we investigate how the magnetic field is distributed at chromospheric heights and check the reliability of the NLFFF modeling. Although previous studies revealed some properties of the chromospheric magnetic field, the field-of-views (FOVs) of their observations were limited because the seeing made it difficult to perform the stable large FOV scanning. This turns out to be important for a reliable comparison between the NLFFF extrapolation and the chromospheric magnetic field. By analyzing the chromospheric magnetic field in whole active regions, we attempt to reveal the non-potential magnetic field distribution in the chromosphere through spectropolarimetric observations at He I 10830 Å and how significantly the magnetic field at the chromospheric height derived by the current NLFFF modeling with photospheric magnetic field is deviated from the measured chromospheric magnetic field.

The paper is organized as follows: The observations are presented in Section 2, the data reduction and the method of NLFFF are described in Section 3. Section 4 presents the results, followed by discussion in Section 5 and the summary in Section 6.

## 2. OBSERVATIONS

### 2.1. *Observations of NOAA 10969*

NOAA active region 10969 was a simple bipolar active region as shown in the upper panels of Figure 1. The leading sunspot has a negative polarity and there are several positive magnetic islands to the east of the sunspot. The Solar Optical Telescope (SOT; [Tsuneta et al. 2008](#); [Shimizu et al. 2008](#); [Suematsu et al. 2008](#); [Ichimoto et al. 2008](#))/Spectropolarimeter (SP; [Lites et al. 2013](#)) aboard the *Hinode* satellite ([Kosugi et al. 2007](#)) measured the full Stokes vector of Fe I 6301.5 Å and 6302.5 Å lines in the period between 11:16 UT and 12:42 UT on 28 Aug 2007. The spectral sampling is 21.5 mÅ per pixel. NOAA 10969 was located close to the disk center, i.e., (111 ″, -184 ″) in the heliocentric coordinate at that time. The map has an effective pixel size of 0″.16 along slit and 0″.15 slit step with the FOV of 152″ × 164″. The Stokes profiles are obtained with 6 rotation cycles (4.8 seconds) of polarization modulator unit.

NOAA 10969 was also observed by the Tenerife Infrared Polarimeter-2 (TIP-2; [Collados et al. 2007](#)) mounted on the German Vacuum Tower Telescope (VTT) at the Observatorio del Teide, Tenerife, Spain, between 10:18-10:38 UT on 28 Aug 2007. The VTT/TIP-2 measured the full Stokes vector around the He I triplet at 10830 Å with a spectral sampling of 11 mÅ per pixel. The exposure time was 0.25 seconds and four accumulations per modulation step were performed. The noise level measured in continuum wavelengths was  $3 \times 10^{-3}$  in units of the continuum intensity. The active region was scanned with a 0″.18 along the slit and steps of 0″.5. We have to note that there might be small magnetic flux which can not be detected in this scanning because the scanning was sparse raster.

For the coronal structure, we observed the region with a spatial resolution of 1″ (0″.5 pixel<sup>-1</sup>) at 171 Å obtained with the *Transition Region and Coronal Explorer* (TRACE; [Handy et al. 1999](#)), which is sensitive to coronal plasma at a temperature around 1 MK.

### 2.2. *Observations of NOAA 11861*

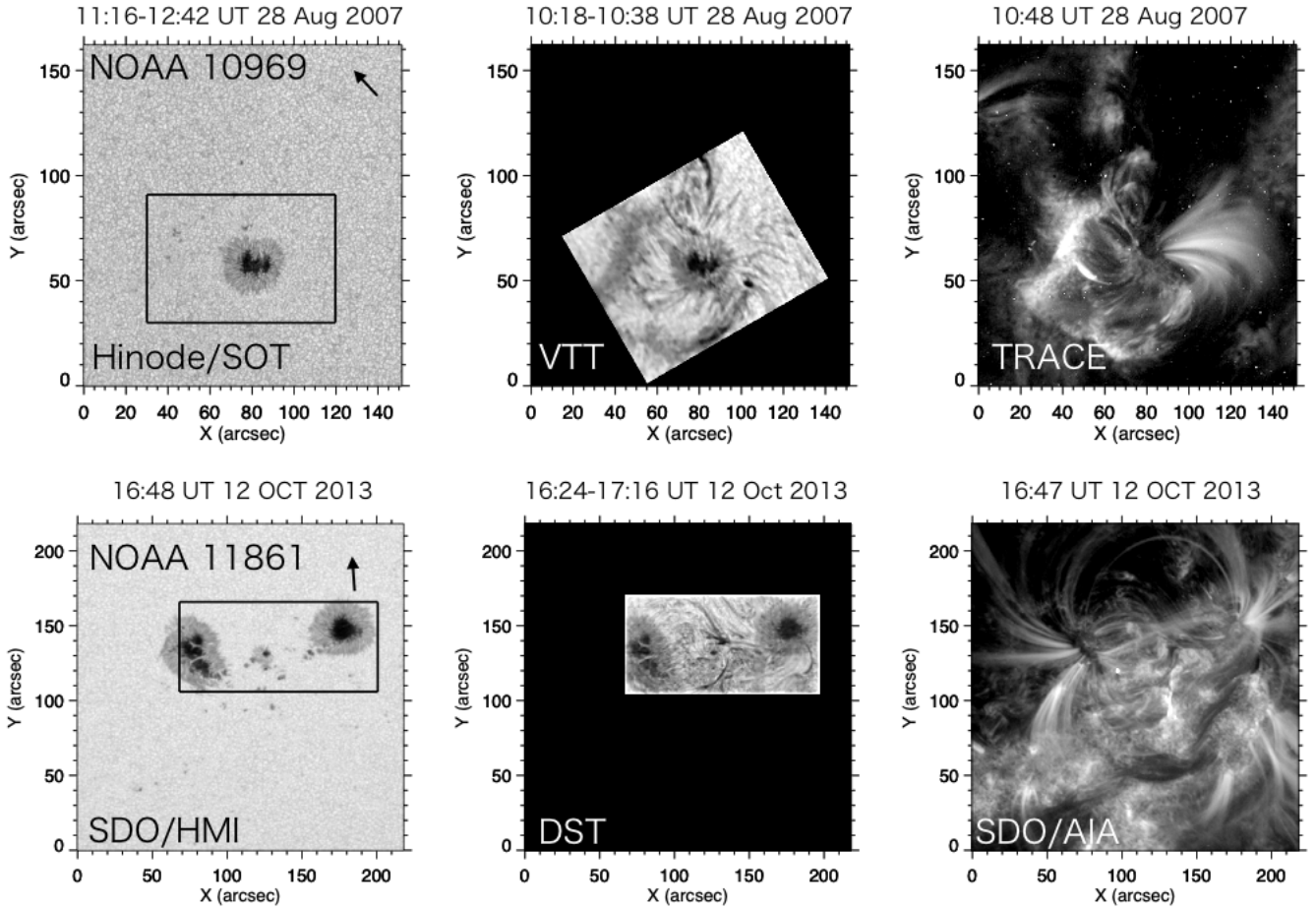


**Figure 1.** Upper left: The continuum image obtained with *Hinode*/SOT SP. The black arrow shows the direction of the disk center. The black box shows the region of interest (ROI) in Figures 2, 4, and 5. Upper middle: The line core image of He I 10830 Å obtained with VTT/TIP-2. Upper right: The EUV image at 171 Å obtained with *TRACE*. Lower left: The continuum image obtained with *SDO*/HMI. The black arrow shows the direction of the disk center. The black box shows the ROI in Figures 3, 7, and 8. Lower middle: The line core image of He I 10830 Å obtained with DST/FIRS. Lower right: The EUV image at 171 Å obtained with *SDO*/AIA.

NOAA active region 11861 had multiple sunspots. The continuum image observed with *SDO*/HMI at 16:48 UT on 12 Oct 2013 is shown in the bottom panel of Figure 1. NOAA 10969 was located close to the disk center, i.e., ( $0''$ ,  $-250''$ ) in the heliocentric coordinate at that time.

The full Stokes vector of He I 10830 Å was obtained by the Facility Infrared Spectropolarimeter (FIRS; Jaeggli et al. 2010) at the Dunn Solar Telescope (DST) located on Sacramento Peak in New Mexico, USA. The FIRS scanned the active region between 16:24 and 17:16 UT on 12 Oct 2013 with a spectral sampling of 39 mÅ per pixel. The active region was scanned with 0."15 along the slit and steps of 0."3, for a total FOV of 132"×66". The exposure time was 0.125 seconds and four accumulations per modulation step were performed. The standard deviation of the continuum intensity was  $1 \times 10^{-2}$ . Because the continuum contains large fringes, the standard deviation of the continuum becomes large. We used images with 0".5 pixel<sup>-1</sup> in the 171 Å channel of the Atmospheric Imaging Assembly (AIA; Lemen et al. 2012) onboard *SDO* as context images for the corona.

### 3. METHOD

#### 3.1. Data Reduction

For the calibration of the *Hinode*/SOT SP data, we used the Solarsoft routine SP\_PREP (Lites & Ichimoto 2013). After the calibration of the spectropolarimetric data, we applied a Milne-Edington inversion by the code based on MELANIE (Socas-Navarro 2001). The 180° ambiguity in the transverse magnetic field direction was solved with the minimum energy ambiguity resolution method (Metcalf 1994; Leka et al. 2009). For the HMI data, we used the vector magnetic field data product, SHARP (Bobra et al. 2014). For the VTT data, flat field, dark current corrections, and the standard polarimetric calibration were carried out (Collados et al. 1999; Collados 2003). The wavelength calibration was also performed by fitting the observed spectrum with the solar spectrum atlas (Delbouille et al. 1981). In order to improve the signal-to-noise ratio, we carried out a binning of 4 pixels in the spectral direction and 4 pixels along the slit direction. The resulting noise levels of stokes  $Q/I$ ,  $U/I$ , and  $V/I$  are, in units of the continuum intensity,  $5.3 \times 10^{-4}$ ,  $6.3 \times 10^{-4}$  and  $7.8 \times 10^{-4}$ , respectively. For the DST data, we carried out the basic data reduction including flat fielding, dark current corrections, polarimetric calibration and wavelength calibration (Beck et al. 2005). Because of the presence of significant polarized fringes in the DST data, we removed them using the pattern-recognition method of Casini et al. (2012). A binning of 2 pixels along the spectral direction and along the slit, and 4 pixels along the scanning direction were carried out. The resulting noise levels of stokes  $Q/I$ ,

$U/I$ , and  $V/I$  are  $1.0 \times 10^{-4}$ ,  $7.2 \times 10^{-5}$  and  $5.4 \times 10^{-4}$ , respectively. An initial incomplete ambiguity resolution is carried out for the chromospheric data assuming that only the  $180^\circ$  ambiguity is present. This is done by choosing the azimuth closer to the potential field extrapolation. We defer a more in-depth discussion about ambiguities of the inversion results to Section 5.

The inversion of the He I 10830 Å multiplet was performed by HAZEL (Asensio Ramos et al. 2008), which considers the joint action of the Hanle and Zeeman effects in a simple slab model with all physical properties constant. Eight parameters describe such slab model of HAZEL; the magnetic field strength, the inclination and azimuth of the magnetic field vector, the optical depth of the slab (measured in the core of the red component), the height above the solar surface at which the slab lies, the Doppler width of the line, the Doppler velocity, and the line damping parameter. In order to reduce the computing time and also to reduce the ambiguity in the solution space, we fix two of these parameters. The first one is the damping parameter, which we fix to zero. The broadening of the He I 10830 Å multiplet is dominated by Doppler broadening and the information to fix the effect of the damping parameter lies in the far wings, which are affected by blends. In addition, Lagg et al. (2004) reported that the inclusion of the damping parameter barely affects the inferred parameters, although it slightly improves the fit. The second parameter is the height of the slab, which we fix to  $2'' \sim 1500$  km in this study. The scattering polarization and Hanle effect depend on the anisotropy of the radiation field. Because the height of the slab increases the anisotropy, the linear polarization signal is slightly affected by the height of the slab (Merenda et al. 2011). However, we find no important change in the inferred parameters even if we modify the height in sensible ranges.

### 3.2. NLFFF Extrapolation

NLFFF calculations were performed by the MHD relaxation method (Inoue et al. 2014), which solves the following set of equations:

$$\frac{\partial \mathbf{v}}{\partial t} = -(\mathbf{v} \cdot \nabla) \mathbf{v} + \frac{1}{\rho} \mathbf{j} \times \mathbf{B} + \nu \nabla^2 \mathbf{v}, \quad (8)$$

$$\frac{\partial \mathbf{B}}{\partial t} = \nabla \times (\mathbf{v} \times \mathbf{B} - \eta \mathbf{j}) - \nabla \phi, \quad (9)$$

$$\mathbf{j} = \nabla \times \mathbf{B}, \quad (10)$$

$$\frac{\partial \phi}{\partial t} + c_h^2 \nabla \cdot \mathbf{B} = -\frac{c_h^2}{c_p^2} \phi. \quad (11)$$

Equations (8), (9) and (10) are the equation of motion, the induction equation, and the Ampère's law, respectively. Eq. (11) follows the procedure developed by [Dedner et al. \(2002\)](#) to force  $\nabla \cdot \mathbf{B} = 0$ , making use of the potential  $\phi$ .  $\rho$  is the pseudo density, which is assumed to be equal to  $|\mathbf{B}|$  to ease the relaxation by equalizing the Alfvén speed in space. We chose the non-dimensional viscosity  $\nu = 10^{-3}$ , which corresponds to  $6 \times 10^5 \text{ m}^2\text{s}^{-1}$  for NOAA 10969 and  $8 \times 10^5 \text{ m}^2\text{s}^{-1}$  for NOAA 11861 in real units. The length and magnetic field were normalized by  $L_0 = 110 \text{ Mm}$  (NOAA 10969) and  $L_0 = 157 \text{ Mm}$  (NOAA 11861) and  $B_0 = 3000 \text{ G}$ , respectively. The numerical domain for the NLFFF extrapolation is set to  $(0, 0, 0) < (x, y, z) < (1.0, 1.07, 0.25)$  resolved by  $504 \times 540 \times 504$  cells for NOAA10969 and  $(0, 0, 0) < (x, y, z) < (1.0, 1.0, 0.75)$  resolved by  $432 \times 432 \times 648$  cells for NOAA 11861.  $x$  and  $y$  are the horizontal directions and  $z$  is the vertical direction. The number of steps in the calculation were set to 40000 for both NOAA 10969 and NOAA 11861. The velocities are normalized to the Alfvén velocity  $V_A \equiv B_0/(4\pi\rho_0)^{1/2}$ , and times to the Alfvén time  $\tau_A \equiv L_0/V_A$ . The density  $\rho_0$  in the Alfvén velocity is set equal to  $B_0$ . The parameters  $c_p^2 = 0.1$  and  $c_h^2 = 0.04$  are the non-dimensional advection and non-dimensional diffusion coefficients, which are assumed constant. The non-dimensional resistivity  $\eta$  is given by

$$\eta = \eta_0 + \eta_1 \frac{|\mathbf{j} \times \mathbf{B}| |\mathbf{v}|^2}{|\mathbf{B}|^2}, \quad (12)$$

where  $\eta_0$  and  $\eta_1$  are fixed at  $5.0 \times 10^{-5}$  and  $1.0 \times 10^{-3}$  in non-dimensional units, respectively. In real units, these values correspond to  $3 \times 10^4 \text{ m}^2\text{s}^{-1}$  and  $6 \times 10^5 \text{ m}^2\text{s}^{-1}$  for NOAA 10969, and  $4 \times 10^4 \text{ m}^2\text{s}^{-1}$  and  $8 \times 10^5 \text{ m}^2\text{s}^{-1}$  for NOAA 11861, respectively. The second term is introduced to accelerate the relaxation to the force-free state.

The bottom boundary is the photospheric magnetic field observed with *Hinode*/SOT SP for NOAA 10969 and *SDO*/HMI for NOAA 11861. The potential field is used as an initial guess for both regions.

### 3.3. Shear Signed Angle

To evaluate the non-potentiality at each height, we use the shear signed angle (SSA), which is defined as

$$\text{SSA} = \tan^{-1} \left( \frac{B_y B_{xp} - B_{yp} B_x}{B_x B_{xp} + B_y B_{yp}} \right). \quad (13)$$

The SSA is the deviation of azimuth angle from the potential magnetic field ( $B_{xp}$  and  $B_{yp}$ ). For the chromospheric magnetic field derived from He I 10830 Å, the SSA is calculated by the potential field calculated from the  $B_z$  at 1500 km height.

## 4. RESULTS

### 4.1. Polarimetric signals of He I 10830 Å

Figure 2 shows the absolute peak values of Stokes  $Q/I$ ,  $U/I$ , and  $V/I$  in NOAA 10969. The signal of Stokes  $V/I$  is strong in the leading sunspot and the magnetic islands of the positive polarities where the vertical magnetic field exists. The strong linear polarization signals can be identified in the outer part of the spot and the fibril structure between the positive and negative polarities, which come from the Zeeman effect and/or the Hanle effect.

Figure 3 shows the absolute peak value of Stokes  $Q/I$ ,  $U/I$ , and  $V/I$  in NOAA 11861. Strong circular polarization signals can be seen in the two large spots and small spot between them. There are strong linear polarization signals in the penumbral regions.

### 4.2. Force-freeness of the Active Regions

Table 1 shows the force-freeness based on the Eqs. (4), (5), and (6) for NOAA 10969 and 11861 at photospheric height. As shown later, there are some pixels where the magnetic field is not derived with sufficient accuracy at the chromospheric height. Therefore, we do not show the force-freeness in the chromosphere in this paper. In terms of the force-freeness at the photosphere, that of NOAA 10969 has  $|F_z|/F_p > 0.1$ , while that of NOAA 11861 satisfies  $|F_x|/F_p < 0.1$ ,  $|F_y|/F_p < 0.1$ , and  $|F_z|/F_p < 0.1$ .

**Table 1.** Force-freeness of the active regions from Equations (4), (5), and (6)

	NOAA 10969	NOAA 11861
$ F_x /F_p$	0.018	0.024
$ F_y /F_p$	0.038	0.071
$ F_z /F_p$	0.43	0.03

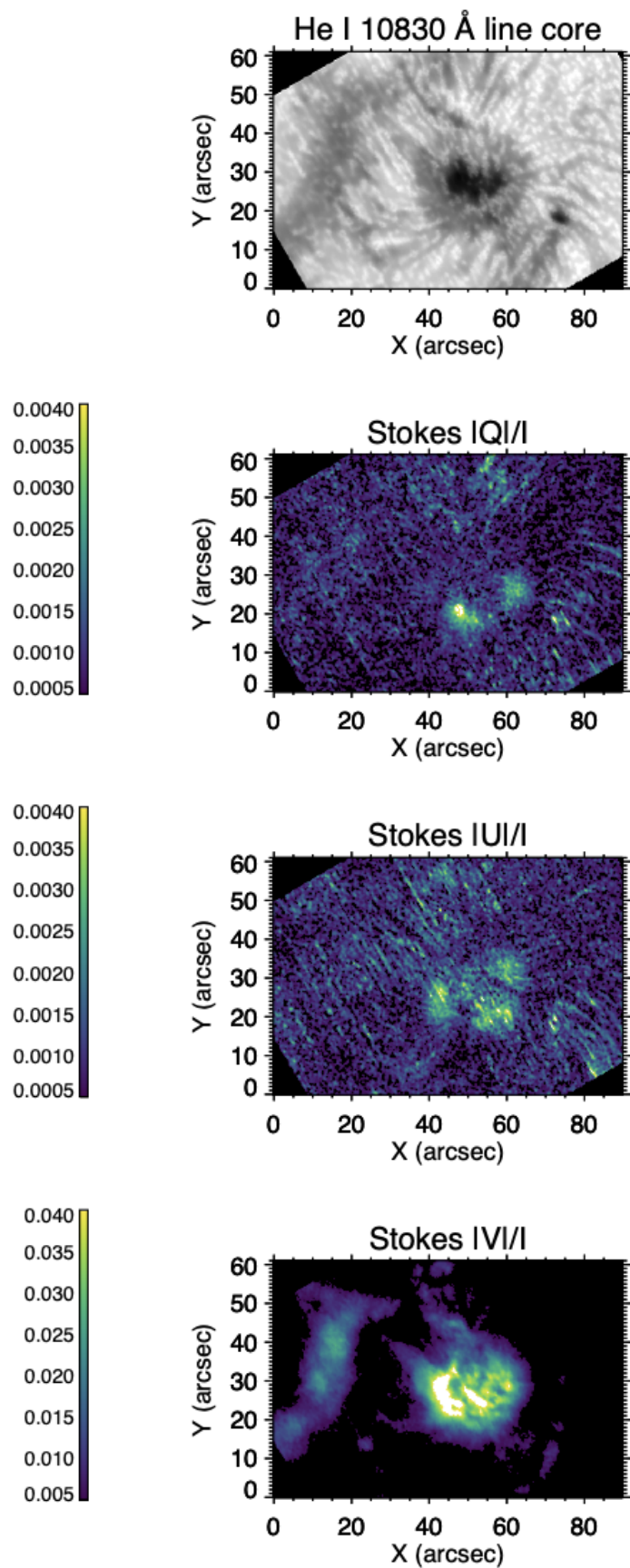


**Figure 2.** The absolute peak value of Stokes Q/I, U/I, and V/I of NOAA 10969 at He I 10830 Å obtained with VTT/TIP-2 between 10:18-10:38 UT on 28 Aug 2007.

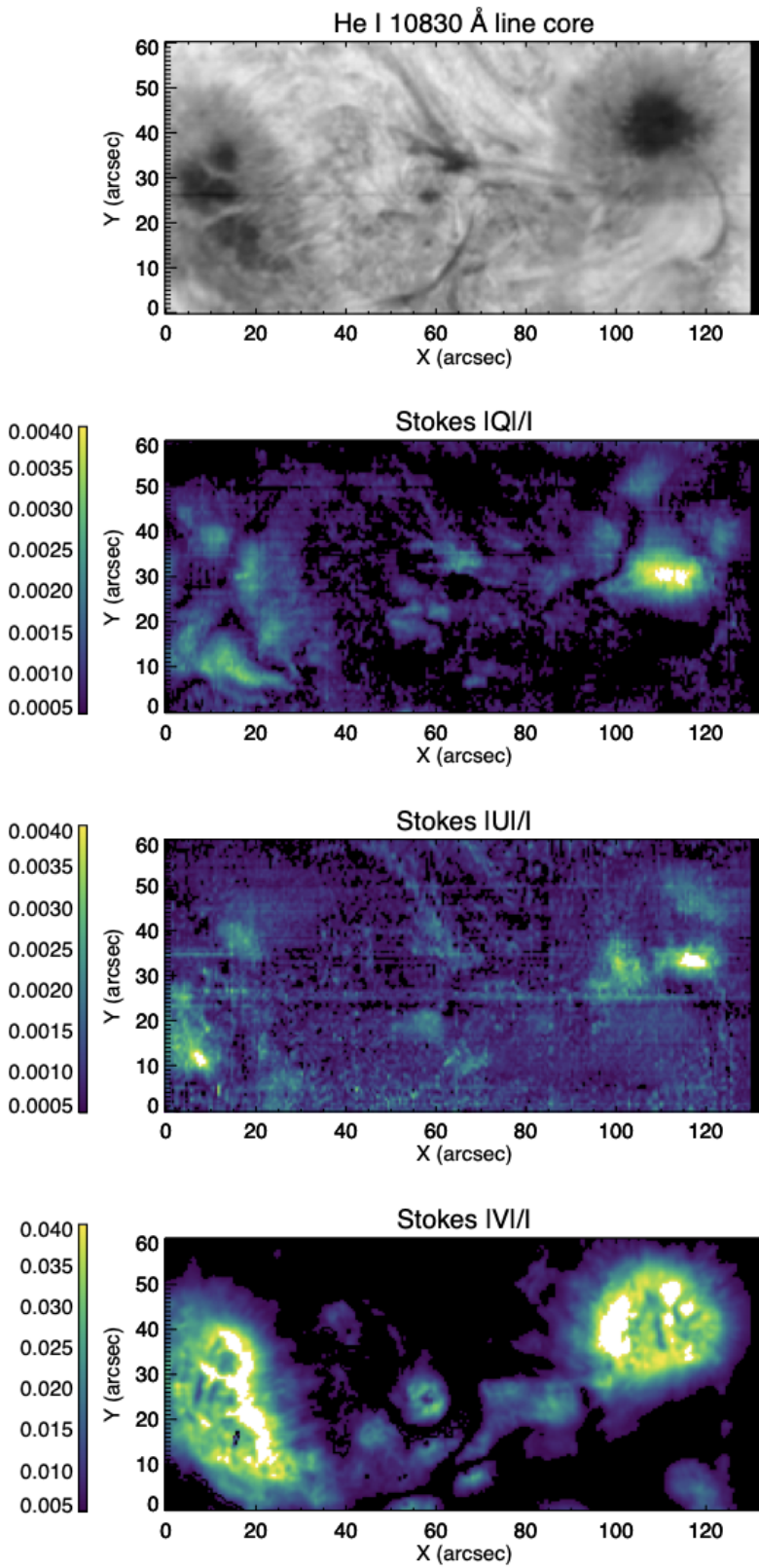


**Figure 3.** The absolute peak value of Stokes  $Q/I$ ,  $U/I$ , and  $V/I$  of NOAA 11861 at He I 10830 Å obtained with DST/FIRS between 16:24 and 17:16 UT on 12 Oct 2013.

### 4.3. Vector Magnetic Fields in the Photosphere and the Chromosphere

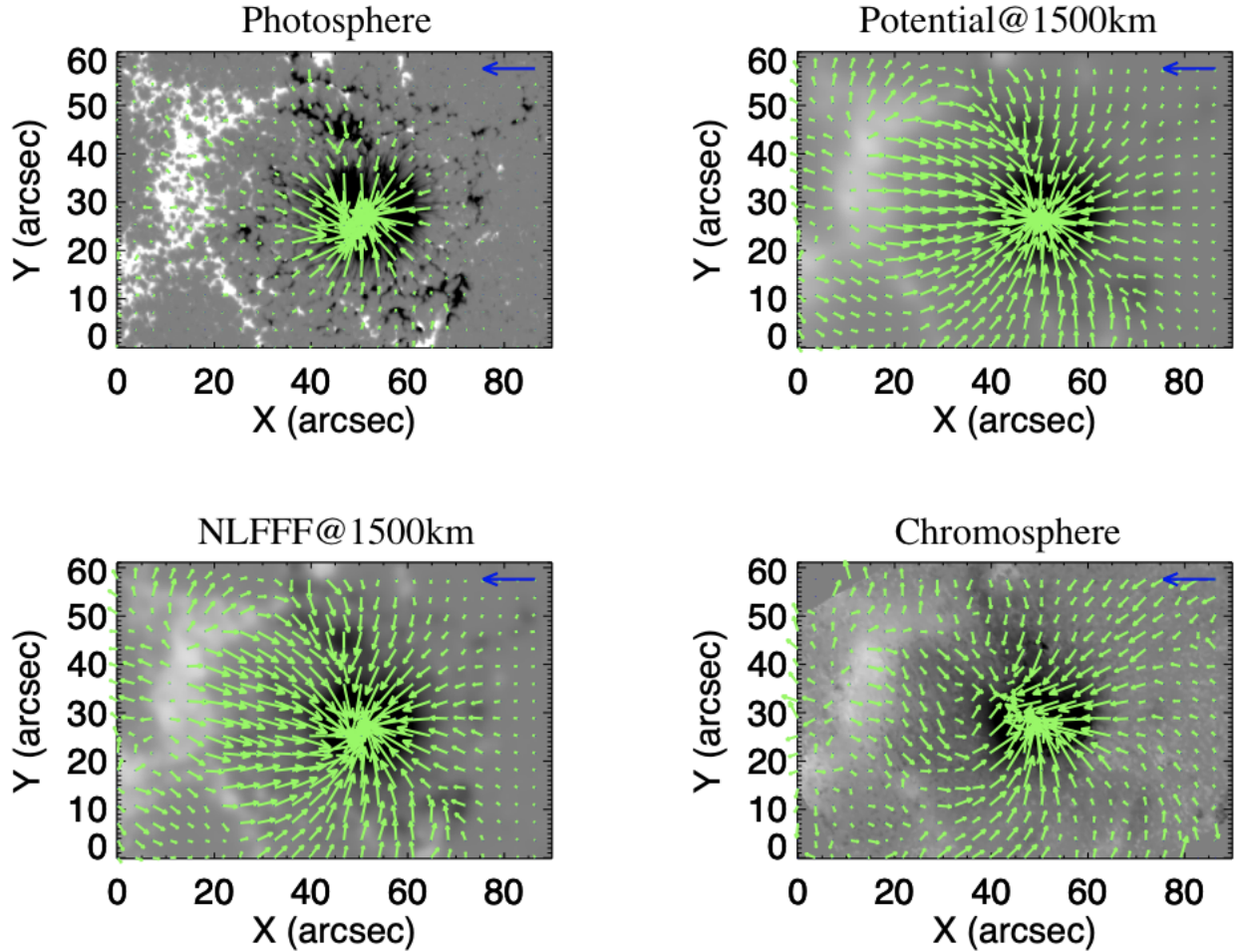
The upper left and lower right panels of Figure 4 show vector magnetic field maps at the photospheric and chromospheric heights in NOAA 10969, respectively. The photospheric magnetic field is obtained from *Hinode* SOT/SP and the chromospheric field is derived from He I 10830 Å observation with the VTT/TIP-2. The background grayscale image shows the vertical component of the magnetic field and the green arrows show the horizontal component of the magnetic field in the local frame. The horizontal magnetic field is displayed with a binning of  $12 \times 12$  pixels.

We only consider those pixels for which the linear polarization signals are higher than 0.12%, to avoid any bias introduced by the noise. Additionally, we only consider those pixels for which the inversion model fulfills

$$\sigma_{QU} = \frac{\frac{1}{n} \sum_{i=1}^n \sqrt{(Q_{\text{obs}} - Q_{\text{syn}})^2 + (U_{\text{obs}} - U_{\text{syn}})^2}}{\sqrt{Q_{\text{peak}}^2 + U_{\text{peak}}^2}} < 0.08, \quad (14)$$

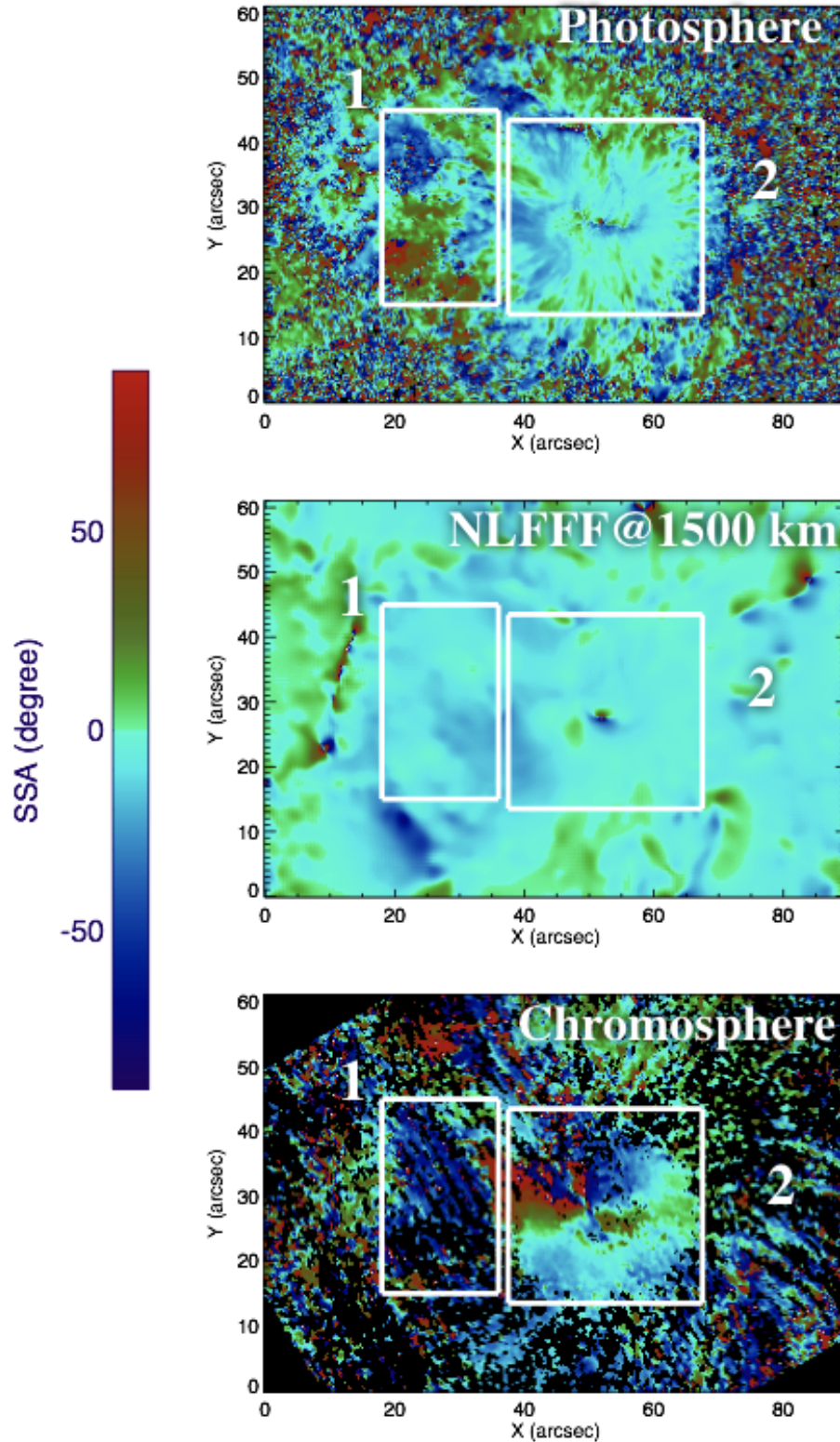
where  $n$  is the number of wavelength points considered during the HAZEL inversion,  $Q_{\text{obs}}$  and  $U_{\text{obs}}$  are the observed Stokes profiles,  $Q_{\text{syn}}$  and  $U_{\text{syn}}$  are the synthetic Stokes profiles,  $Q_{\text{peak}}$  and  $U_{\text{peak}}$  are the peak values of the linear polarization. The pixels for which the linear polarization signals are small ( $< 0.12\%$ ) or the fitting is poor ( $\sigma_{QU} > 0.08$ ), are treated as missing data. At photospheric height, strong horizontal magnetic fields are located in the negative sunspot. The horizontal magnetic field in the sunspot is almost radial emerging from the center of the sunspot. On the other hand, the horizontal magnetic field is uniformly distributed at chromospheric heights and a twisted structure in a counterclockwise direction between positive and negative polarities can be seen.

Figure 5 shows the spatial distribution of the SSA. The top panel shows the SSA derived from Fe I 6302 Å observations with *Hinode*/SOT SP, whereas the bottom panel shows the SSA derived from He I 10830 Å observations with VTT. At chromospheric heights, the pixels where the linear polarization signal is weak and the inversion did not fit the profiles well were masked and displayed in black colors. We focus on two regions (boxes 1 & 2), where the chromospheric magnetic field is accurately derived. Box 1 represents the region around the polarity inversion line and box 2 is above the sunspot with negative polarity. Figure 6 shows the histograms of the SSA in both boxes. The black and red solid lines show the



**Figure 4.** The vector magnetic field map of NOAA 10969. The gray scale shows the vertical magnetic field and the green arrows show the horizontal magnetic field. The length of blue arrow shows the field strength of 1500 G. Upper Left: Photospheric magnetic field observed with *Hinode*/SOT SP. Upper right: Potential field at 1500 km height. Lower left: NLFFF at 1500 km height. Lower right: Chromospheric magnetic field observed with VTT/TIP-2.

SSA from the chromospheric magnetic field derived from He I 10830 Å and the photospheric magnetic field, respectively. A clear deviation from potentiality is detected in box 1. While the peak value of the SSAs in the chromosphere in box 1 is around  $-50^\circ$ , the SSAs at photospheric heights peak around  $0^\circ$  although with a very broad distribution when compared to that of the NLFFF extrapolation. The SSAs both in the chromosphere and in the photosphere peak around  $0^\circ$  for box 2. However, while the SSAs at chromospheric heights in box 2 display a broad distribution, those in the photosphere are much more concentrated around the mean value.



**Figure 5.** The spatial distribution of signed shear angle (SSA) for NOAA 10969. From the top to the bottom for the photosphere, NLFFF at 1500km, chromosphere ( $\text{He I } 10830 \text{ \AA}$ ). The regions where the LP signal is weak and the inversion did not fit the profiles well were masked by black color in the bottom panels.

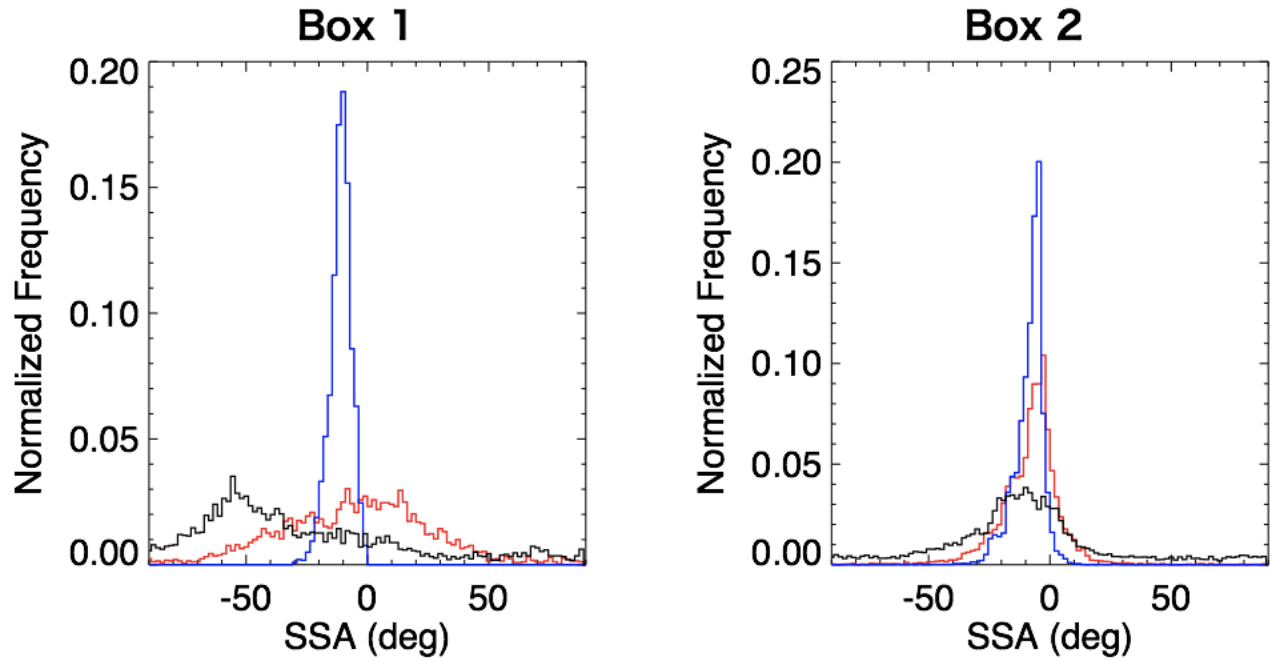


**Figure 6.** The histograms of the SSA in the box 1 and box 2 in Figure 5. The black, red, and blue solid lines show the SSA from the chromospheric magnetic field derived from He I 10830 Å, the photospheric magnetic field, the NLFFF at the 1500 km height, respectively.

Concerning NOAA 11861, the chromospheric magnetic field also shows larger non-potentiality than the photosphere. Figure 7 shows the spatial distribution of the vector magnetic field. The upper left and lower right panels show the photospheric field observed with *SDO/HMI* and the chromospheric field derived from the He I 10830 Å observation with the *DST/FIRS*, respectively. The results of NOAA 10969 share some similarities with those of NOAA 11861. The horizontal magnetic field in the chromosphere looks more twisted compared to that of the photosphere in both the negative and positive sunspots. The difference between photospheric and chromospheric non-potentiality can be seen in Figure 8. The top and bottom panels show the SSA at the photospheric and chromospheric heights, respectively. The boxes 3 and 4 are located in the leading and following sunspots, respectively. Figure 9 shows the histogram of the SSA in both boxes. In box 3 the SSAs in the chromosphere have mainly positive values while that of the photosphere peaks around  $0^\circ$ . In box 4, the photosphere displays SSAs peaking around  $-20^\circ$  while this increases in absolute value to  $-40^\circ$  for the chromosphere.

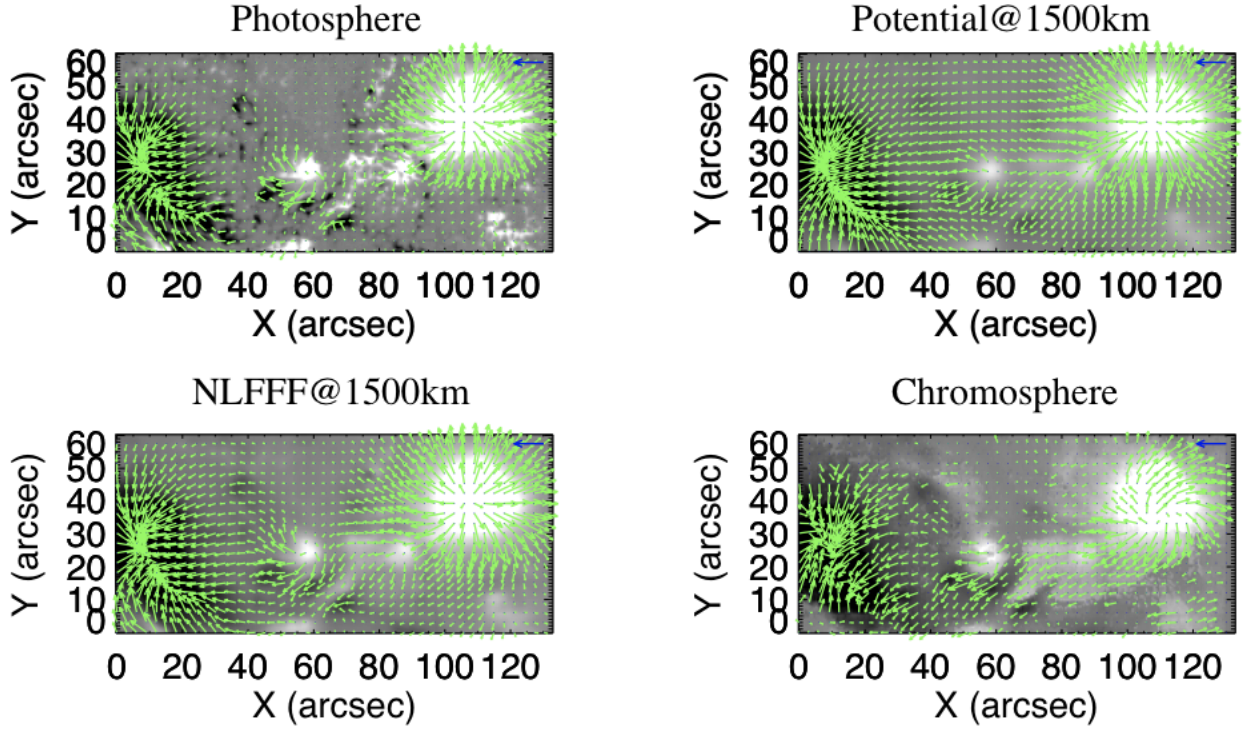


**Figure 7.** Vector magnetic field distributions in NOAA 11861. The gray scale shows the vertical magnetic field and the green arrows show the horizontal magnetic field. The length of blue arrow shows the field strength of 1500 G. Upper Left: Photospheric magnetic field observed with *SDO/HMI*. Upper right: Potential field at 1500 km height. Lower left: NLFFF at 1500 km height. Lower right: Chromospheric magnetic field observed with *DST/FIRS*.

#### 4.4. Comparison with NLFFF at chromospheric heights

We compare the field obtained with the NLFFF extrapolation with that inferred from the spectropolarimetric observations. For the case of NOAA 10969, the upper right and lower left panels in Figure 4 show the potential field at 1500 km above the photosphere derived from the observed photospheric field and the NLFFF, respectively. The NLFFF at 1500km height displays horizontal magnetic fields very close to that of the potential extrapolation, pointing to a small degree of non-potentiality at photospheric heights. However, the chromospheric magnetic field derived from the inversion of the Stokes profiles on the He I 10830 Å multiplet shows a clear non-potential magnetic field vector especially in the region between the positive and negative polarities. Figure 10 shows the joint probability distribution function (JPDF) between the cartesian

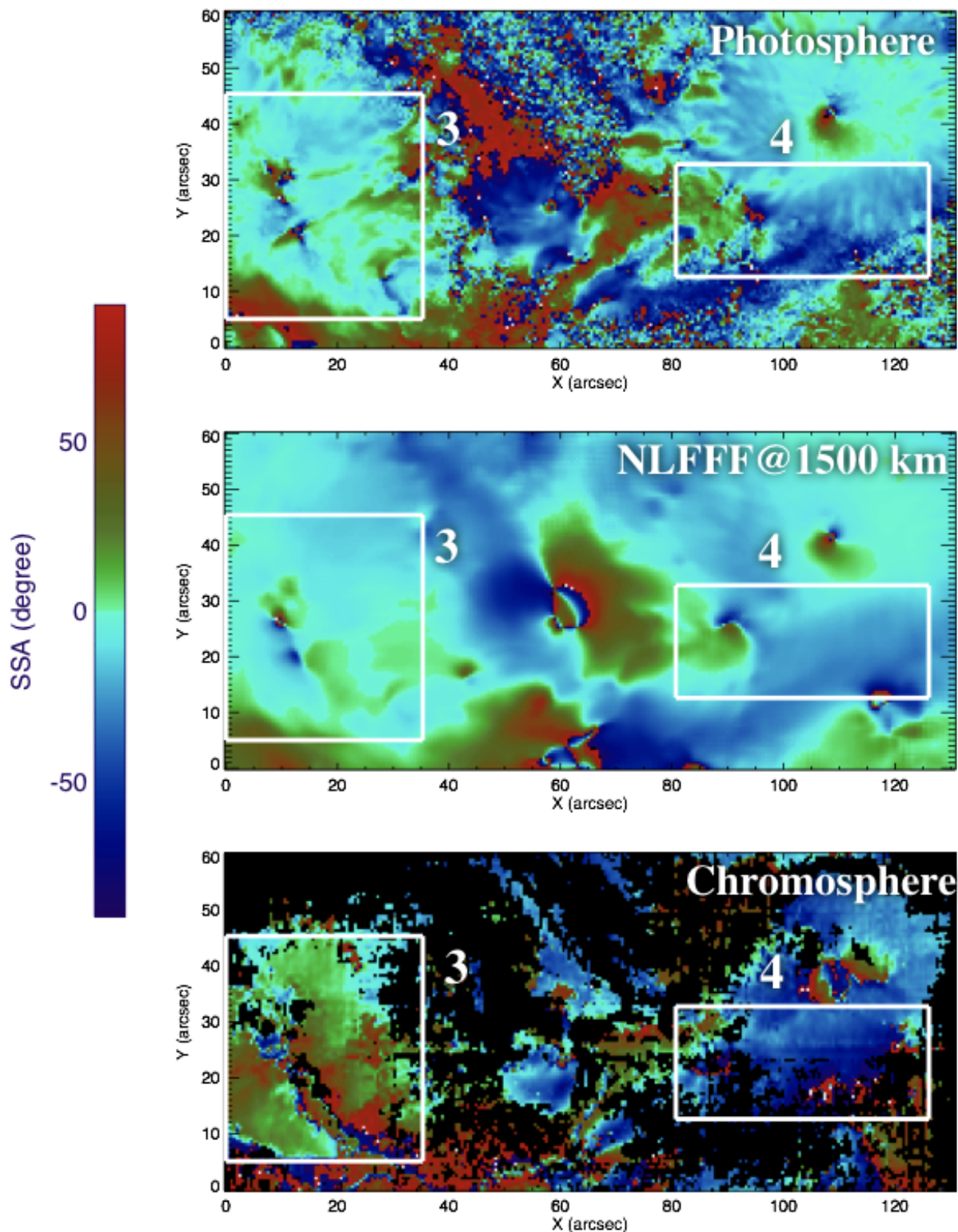


**Figure 8.** The spatial distribution of signed shear angle (SSA) for NOAA 11861. From the top to the bottom for the photosphere, NLFFF at 1500km, chromosphere ( $\text{He I } 10830 \text{ \AA}$ ). The regions where the LP signal is weak and the inversion did not fit the profiles well were masked by black color in the bottom panels.

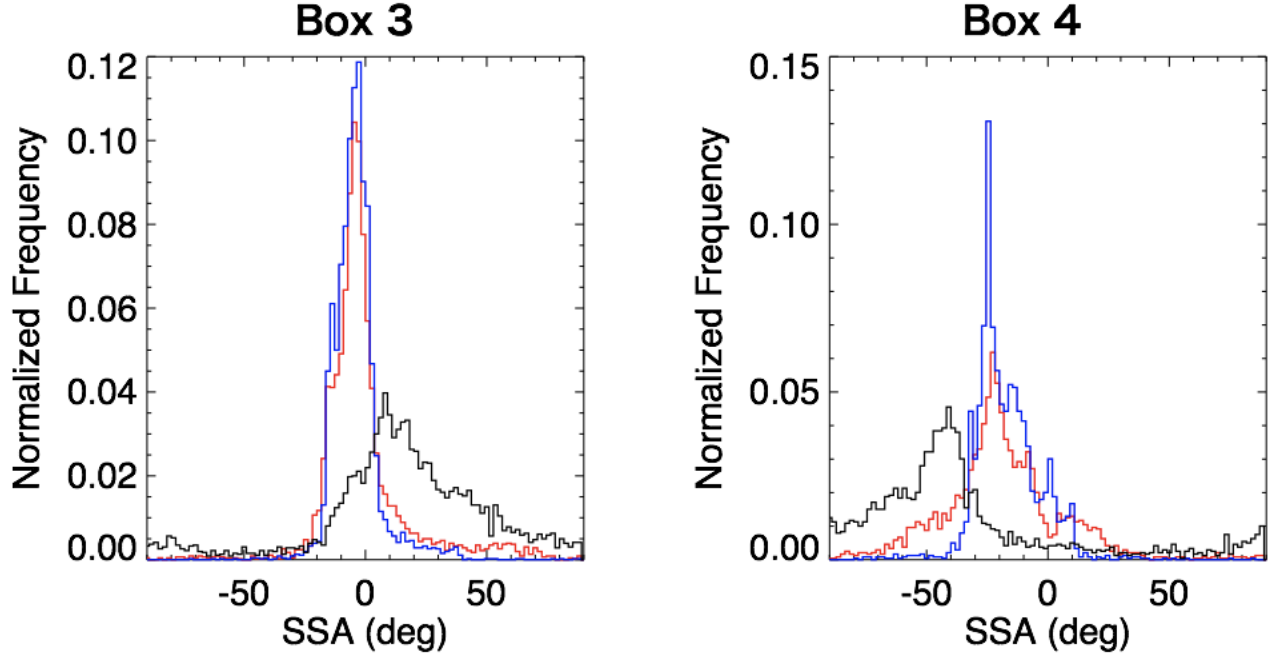


**Figure 9.** The histograms of the SSA in the box 3 and box 4 in Figure 8. The black, red, and blue solid lines show the SSA from the chromospheric magnetic field derived from He I 10830 Å, the photospheric magnetic field, the NLFFF at the 1500 km height, respectively.

components of the magnetic field ( $B_x$ ,  $B_y$ , and  $B_z$ ) from NLFFF at 1500 km above the photosphere and that inferred from the spectropolarimetric observations. A good correlation in  $B_z$  is present, with a Pearson correlation coefficient of  $C = 0.94$ . The absolute values of  $B_z$  derived from the He I data are slightly smaller than those inferred from the NLFFF extrapolation. On the other hand, the horizontal magnetic field ( $B_x$  and  $B_y$ ) shows comparatively weaker correlations,  $C = 0.77$  and  $0.69$ , respectively. We find larger (negative) values of  $B_x$  inferred from He I 10830 Å when  $B_x < -500$  G than those obtained from the extrapolation. Similarly, we also find larger (positive) values of  $B_y$  inferred from He I 10830 Å when  $B_y > 500$  G than those obtained from the extrapolation. Strong horizontal magnetic fields, i.e.,  $(B_x^2 + B_y^2)^{1/2} > 500$  G, are located at the outer part of the sunspot, so our results suggest that these regions have stronger horizontal magnetic fields than those derived from the NLFFF modeling.

When we compare only small SSA pixels ( $|\text{SSA}| < 5$  degree in chromospheric magnetic field from He I 10830 Å), the correlation coefficient of horizontal magnetic field tends to increase,  $C = 0.86$  for  $B_x$  and  $C = 0.77$  for  $B_y$ . This is because the results of the NLFFF do not overestimate the SSA. The field strength

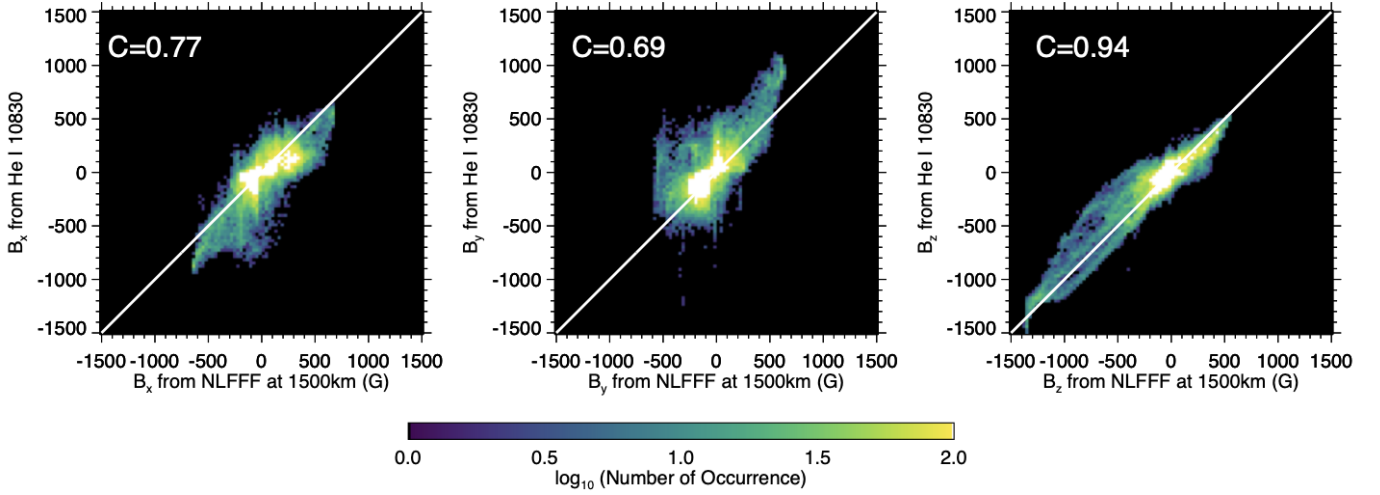


**Figure 10.** The number density plots of the relation in  $B_x$ ,  $B_y$ , and  $B_z$  between NLFFF at 1500 km height and chromospheric magnetic field derived from He I 10830 Å in NOAA 10969. This density plot is created with all pixels ( $\sigma_{\text{qu}} < 0.08$ ).

of horizontal and vertical field is not necessarily the same in some pixels. Because the field strength has a dependency on the comparison height, the correlation coefficient also depends on the comparison height.

In terms of the SSA, the NLFFF is clearly more potential than that derived from the He I 10830 Å observations as shown in the middle and bottom panels of Figure 5. This is also very clear from the blue histograms displayed in Figure 6. They peak at  $-10^\circ$  for box 1 and close to  $0^\circ$  for box 2, both of them being much more narrow.

Concerning NOAA 11861, the upper right panel and lower left panel of Figure 7 show the potential field and the NLFFF extrapolation at the 1500 km above the photosphere. While both show similar horizontal magnetic fields, small deviations can be identified around the center of the region of interest (ROI),  $(x, y) \sim (50, 20)$ . A comparison with the chromospheric field inferred from He I 10830 Å yields clear differences. The positive leading spot in the west side of the FOV in the box 3 shows a clear clockwise twist in the horizontal field from He I 10830 Å that is absent from the NLFFF extrapolation. Figure 11 shows the JPFDs for the cartesian components of the magnetic field. Similar to NOAA 10969,  $B_z$  displays a tight correlation ( $C = 0.98$ ), while the horizontal components show weaker correlations ( $C = 0.76$  for  $B_x$  and  $0.70$  for  $B_y$ ). The strong vertical magnetic fields ( $|B_z| > 1000$  G) appear even stronger in the NLFFF case.

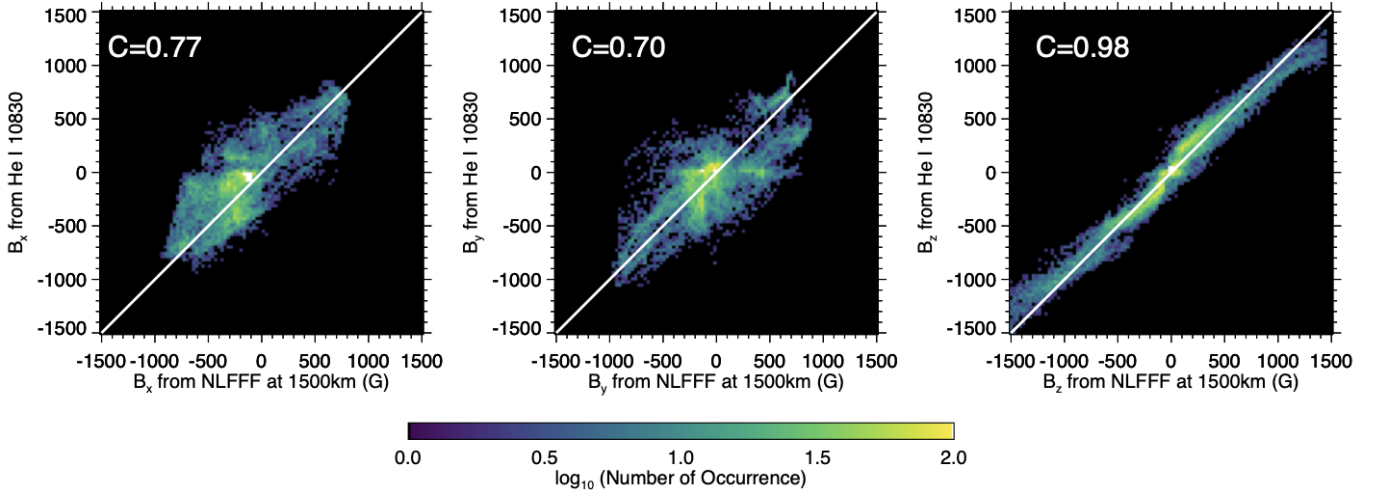


**Figure 11.** The number density distribution in  $B_x$ ,  $B_y$ , and  $B_z$  of the relation between NLFFF at 1500 km height and chromospheric magnetic field derived from He I 10830 Å in NOAA 11861. This density plot is created with all pixels ( $\sigma_{qu} < 0.08$ ).

There is apparently no systematic bias in the horizontal components of the field, probably a consequence of the much larger dispersion.

The histogram of the SSAs of the NLFFF is shown in blue solid in Figure 9. The histogram of the NLFFF at 1500 km is similar to that of the photospheric magnetic field. The SSAs in the chromosphere have mainly positive values in box 3 while that of NLFFF is around  $0^\circ$  or negative. For box 4, the NLFFF extrapolation peaks at  $-20^\circ$ , while the one inferred from observations peaks around  $-40^\circ$ .

In summary, our analysis clearly indicates that the NLFFF extrapolation severely underestimates the non-potentiality of the magnetic field at chromospheric heights.

#### 4.5. Coronal Loop Structures in Comparison with the Extrapolated Fields

Figure 12 shows the qualitative comparison of coronal field lines in NOAA 10969. The upper left panel shows an EUV image from *TRACE* at 171 Å. The yellow lines in the panel delineate the loops (arguably magnetic field lines) manually extracted by visual inspection. The upper right panel shows the vertical magnetic field in the photosphere obtained with *Hinode* SOT/SP with the same FOV. The green solid lines overlaid on the *TRACE* image in the lower panels show field lines estimated from the potential field (bottom left) and NLFFF (bottom right) extrapolations. The field lines are randomly selected in the computation

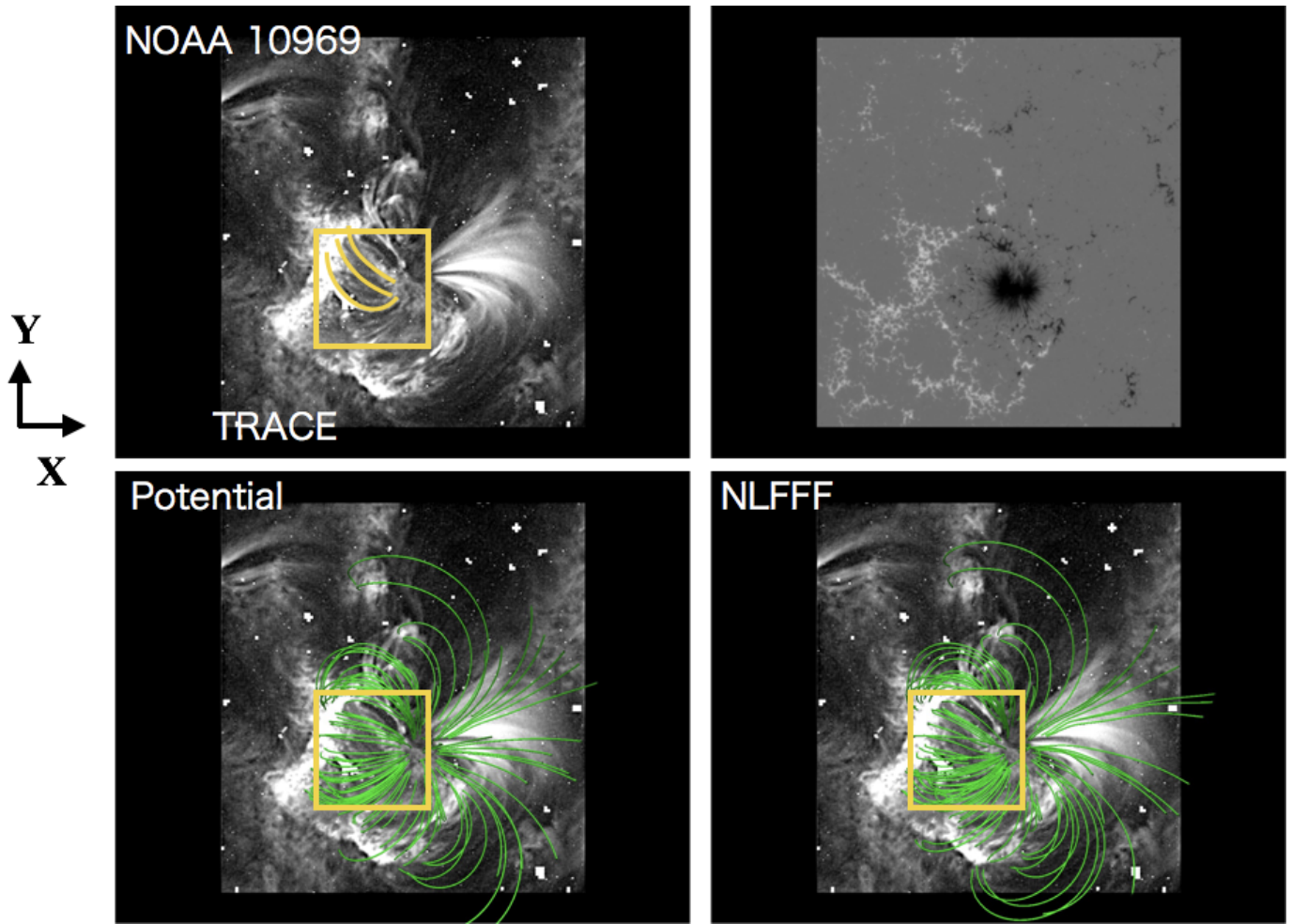


**Figure 12.** The coronal magnetic field lines in NOAA 10969 extracted from an EUV 171 Å image by visual inspection (upper left), compared with the potential field lines (lower left) and NLFFF (lower left) based on the photospheric magnetic field (upper right).

box. The field lines of both extrapolations show similar morphologies. However, there is a clear deviation with those that we trace on the EUV image.

Concerning NOAA 11861, Figure 13 shows the qualitative comparison. Unlike the case of NOAA 10969, there is a clear difference between the potential and NLFFF extrapolations in the yellow box. The NLFFF field lines display a twisted structure that is absent in the potential extrapolation. A somehow similar twist is found in the EUV image. As a consequence, the NLFFF qualitatively reproduces the 3D structure of the magnetic field in this case.

#### 4.6. Relation between Chromospheric Vector Magnetic Fields and Fibril Structures

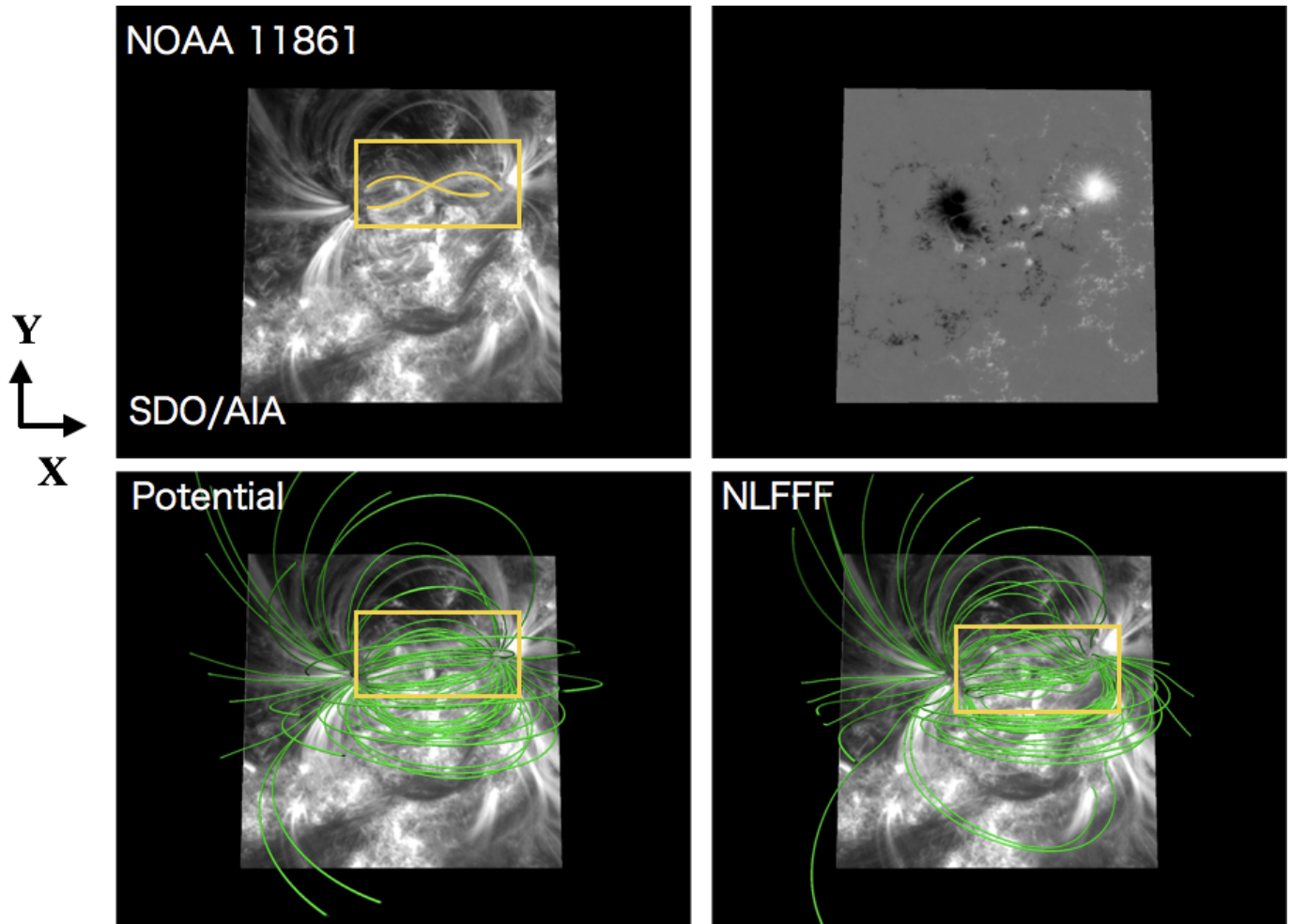


**Figure 13.** Similar to Figure 12, but for NOAA 11861.

It is important to validate the results of the inferred chromospheric magnetic field with the fibrillar structure seen in monochromatic images at the core of He I 10830 Å multiplet. These structures, that can be seen in the upper middle panel of Figure 1, are dark fibrils found around the sunspot. It is often assumed that the magnetic field is aligned with the fibril structures. Although theoretical and observational studies suggest that there is a misalignment due to partially ionization effects (de la Cruz Rodríguez & Socas-Navarro 2011; Martínez-Sykora et al. 2016; Asensio Ramos et al. 2017), Schad et al. (2013) shows that the fibril structures are often well aligned with magnetic field. Figure 14 shows the comparison between the inferred magnetic field and the chromospheric features seen in the core of He I 10830 Å for regions inside box 1. The image in the upper panel shows the intensity at the line core of He I 10830 Å. The four green lines show the fibrils automatically detected by the OCCULT-2 code (Aschwanden et al. 2013). The lower four panels show the

angle between the fibrillar structure and the magnetic field vector along each fibrillar structure. In each plot we display the angle between the fibril and the inferred magnetic field (in black lines with symbols), the NLFFF extrapolation (blue lines) and the potential extrapolation (red lines) at 1500 km. Except for fibril 1, the magnetic field vectors derived from He I 10830 Å are very well aligned with the fibrils. The misalignment between the fibril and the extrapolations can easily reach 50°.

#### 4.7. Height dependence

Although the formation layer of He I 10830 Å is considered to be thin in chromospheric structures, the formation height of He I 10830 Å may vary by a large margin (hundreds or even thousands of km) depending on the locations of the active regions. Although we have used all extrapolations at 1500 km, there is a possibility that a fair comparison would require to use different heights. To test this, Figure 15 shows what happens when the extrapolations are computed at different heights between 0 and 10 Mm. These results show that the difference between the extrapolated and measured magnetic fields remains even when different heights are considered.

## 5. DISCUSSIONS

In this paper, the vector magnetic field observations at both photospheric and chromospheric heights suggest that the chromospheric magnetic field may have larger non-potentiality than the photospheric magnetic field. [Joshi et al. \(2017\)](#) also investigated photospheric and chromospheric magnetic fields of two simple round sunspots by using the Si I 10827 Å and He I 10830 Å lines and suggested the possibility that the chromospheric magnetic field has a larger twist compared to the photospheric magnetic field. Our study has extended their view by examining the entire active regions, not restricted to a simple sunspot. Large FOV observations allow us to identify twisted structures more clearly as shown in Figures 4 and 7. [Yelles Chaouche et al. \(2012\)](#) also extrapolated the 3D magnetic field from both the photosphere and chromosphere. While they performed qualitative comparison of the 3D structure of the field lines, we have quantitatively compared the non-potentiality of the magnetic field measured by the SSA. Compared with the measurements of the chromospheric magnetic field, we revealed that the NLFFF modeling may underestimate the non-potentiality both in active regions NOAA 10969 and 11861. We have to note that the NLFFF extrapolation

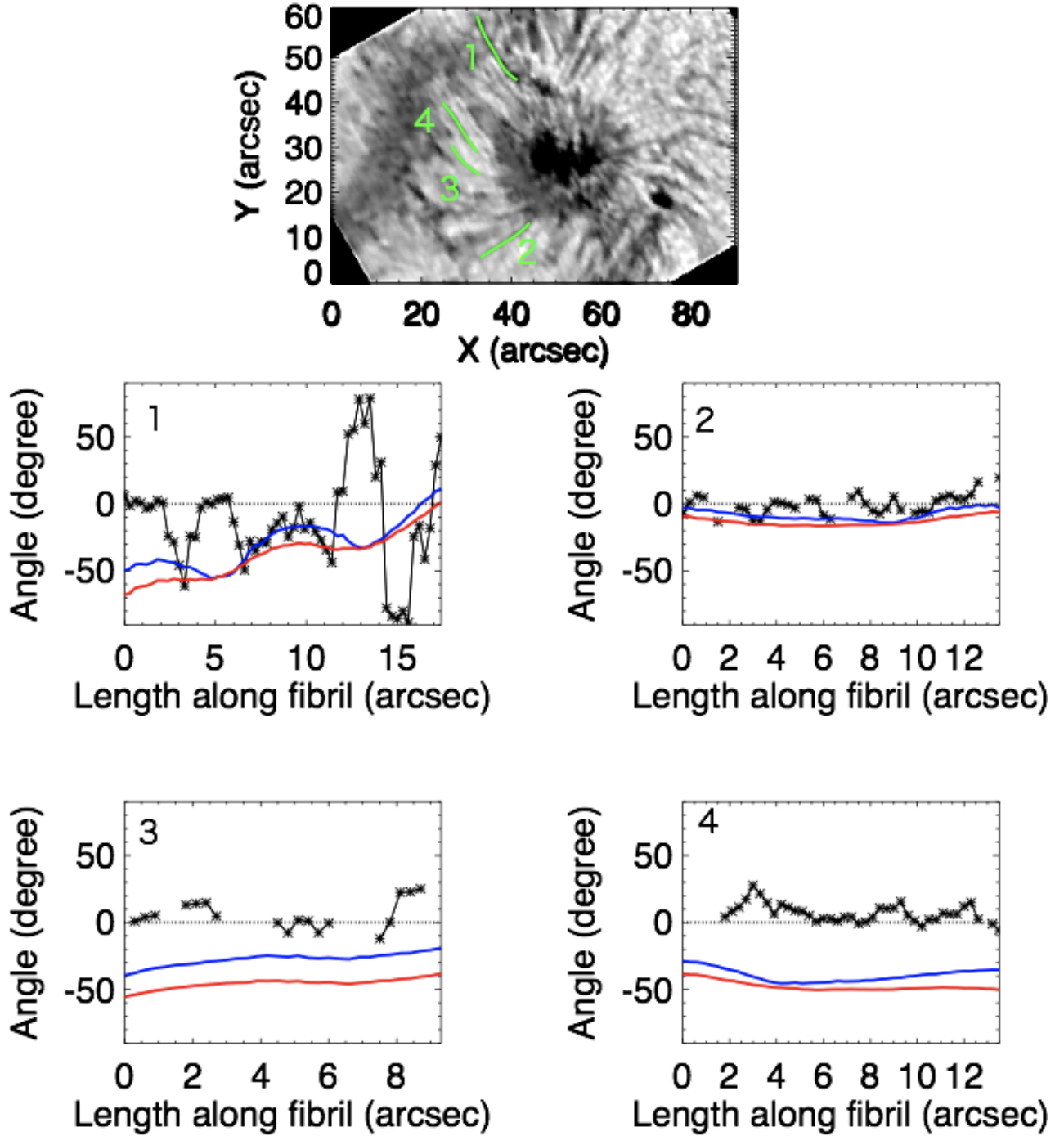


**Figure 14.** The comparison between fibrillar structures and magnetic field vector. Upper panel: The line core image of He I 10830 Å. Four green lines show the fibril structures automatically detected by OCCULT-2 code (Aschwanden et al. 2013). Lower four panels: The angle between the fibril structures and magnetic field vector along the fibril structures. Black lines with asterisks, blue, and red lines show angles made by fibril structures with the chromospheric magnetic field (He I 10830Å), the NLFFF at 1500 km, and the potential field at 1500 km, respectively.

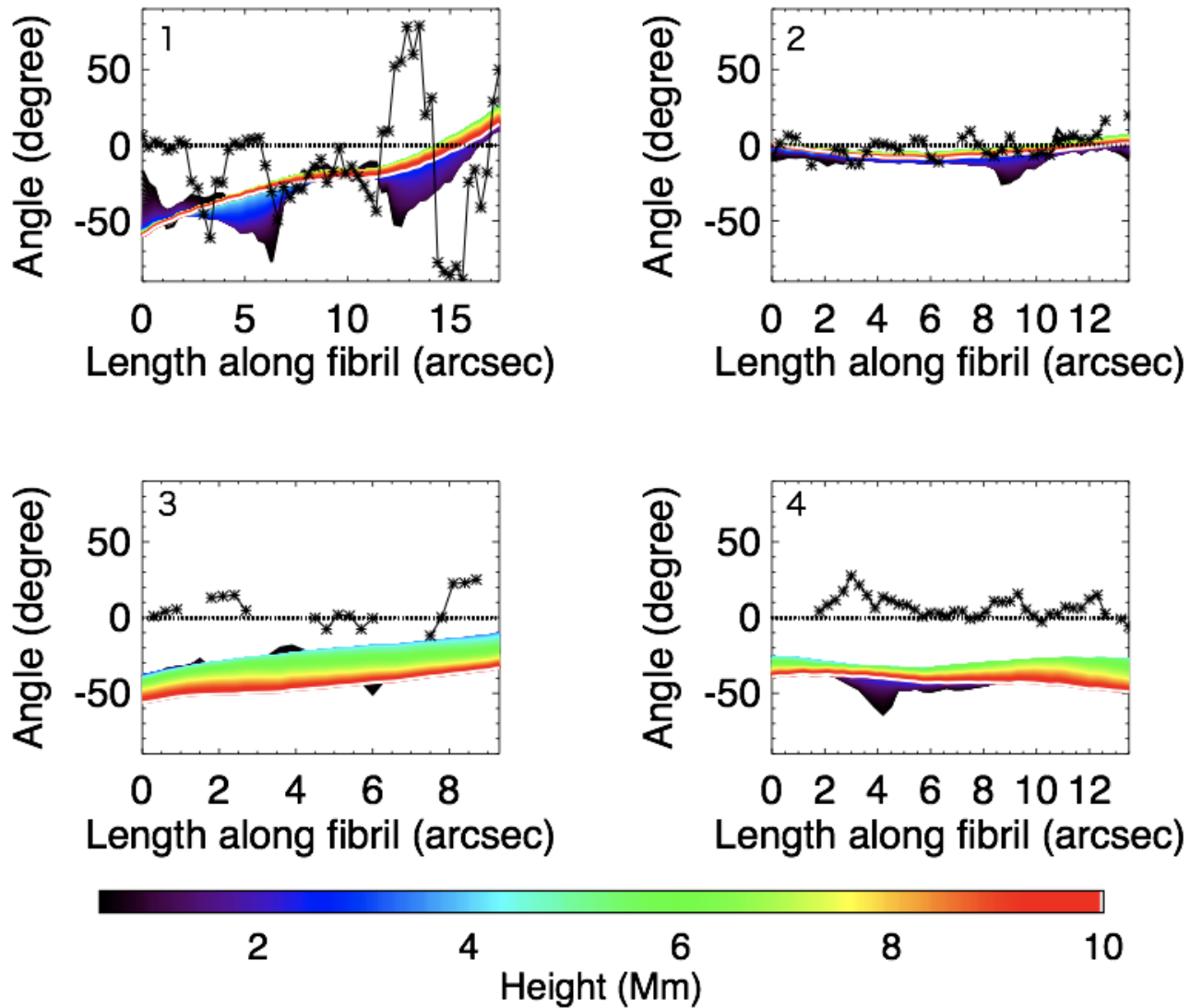


**Figure 15.** Height dependence of magnetic field azimuth. Similar to Figure 14, each panel shows the angle between magnetic field vector and fibril structures. Color shows the angle between NLFFF at the height of 0-10 Mm and fibril structures. Black solid lines with stars show the angle between magnetic field vector from He I 10830 Å and the fibril structures.

may depend on the method used even with the same photospheric boundary condition (DeRosa et al. 2009). The possibility of the extrapolation method dependency can not be rejected in this study and remained for future works.

It is mandatory to discuss the possible influence of the azimuth ambiguities in our study. Apart from the well-known  $180^\circ$  ambiguity, which is also present in the transverse Zeeman effect (Landi Degl'Innocenti & Landolfi 2004), a second type of ambiguity, termed Van Vleck ambiguity (Landi Degl'Innocenti & Landolfi 2004; Asensio Ramos et al. 2008) appears. The Van Vleck ambiguity occurs only as a consequence of the Hanle effect. In this case, potentially up to four (at  $\pm 90^\circ$  and  $\pm 180^\circ$ ) possible azimuths in the plane of the sky can lead to the same polarimetric signal. Obviously, the Van Vleck ambiguity disappears when the linear polarization signals are dominated by the transverse Zeeman effect, such as in the edge of sunspots. On the contrary, the Van Vleck ambiguity may exist in the other regions. We checked the validity of the azimuth for such pixels by comparing with the fibril structures as shown in Figure 14.

There are two possibilities to cause the underestimation of the non-potentiality when using NLFFF modeling. The first cause is the vertical gas pressure gradient in the lower atmosphere, which is related to the non-force-freeness in the photosphere. Parker (1974) investigated the radial expansion of a magnetic flux tube due to the decrease of the gas pressure with height, as shown in Figure 16. The conservation of the longitudinal magnetic flux gives

$$B_{lz}rdr = B_{uz}RdR, \quad (15)$$

where  $B_{lz}$  and  $B_{uz}$  are the longitudinal magnetic fields at the lower and upper atmospheres, respectively, and  $r$  and  $R$  are the radial distances from the axis at the lower and upper atmospheres, respectively. The conservation of the torque of the azimuthal Maxwell stress yields

$$r(B_{l\phi}B_{lz})rdr = R(B_{u\phi}B_{uz})RdR, \quad (16)$$

where  $B_{l\phi}$  and  $B_{u\phi}$  are the azimuthal magnetic fields at the lower and upper atmospheres, respectively. Combining these two equations, one can calculate the ratio between  $T_u$  and  $T_l$ , the number of turns per unit length for torsional equilibrium at the upper and lower atmospheres, respectively:

$$\begin{aligned} \frac{T_u}{T_l} &= \frac{B_{u\phi}/(2\pi RB_{uz})}{B_{l\phi}/(2\pi rB_{lz})}, \\ &= \frac{r}{R} \frac{dR}{dr}. \end{aligned} \quad (17)$$

Assuming that the expansion rate of the flux tube becomes larger at the large radius,  $R/r < dR/dr$ , the number of turns per unit length becomes larger at the upper atmosphere,  $T_u/T_l > 1$ . This means that the

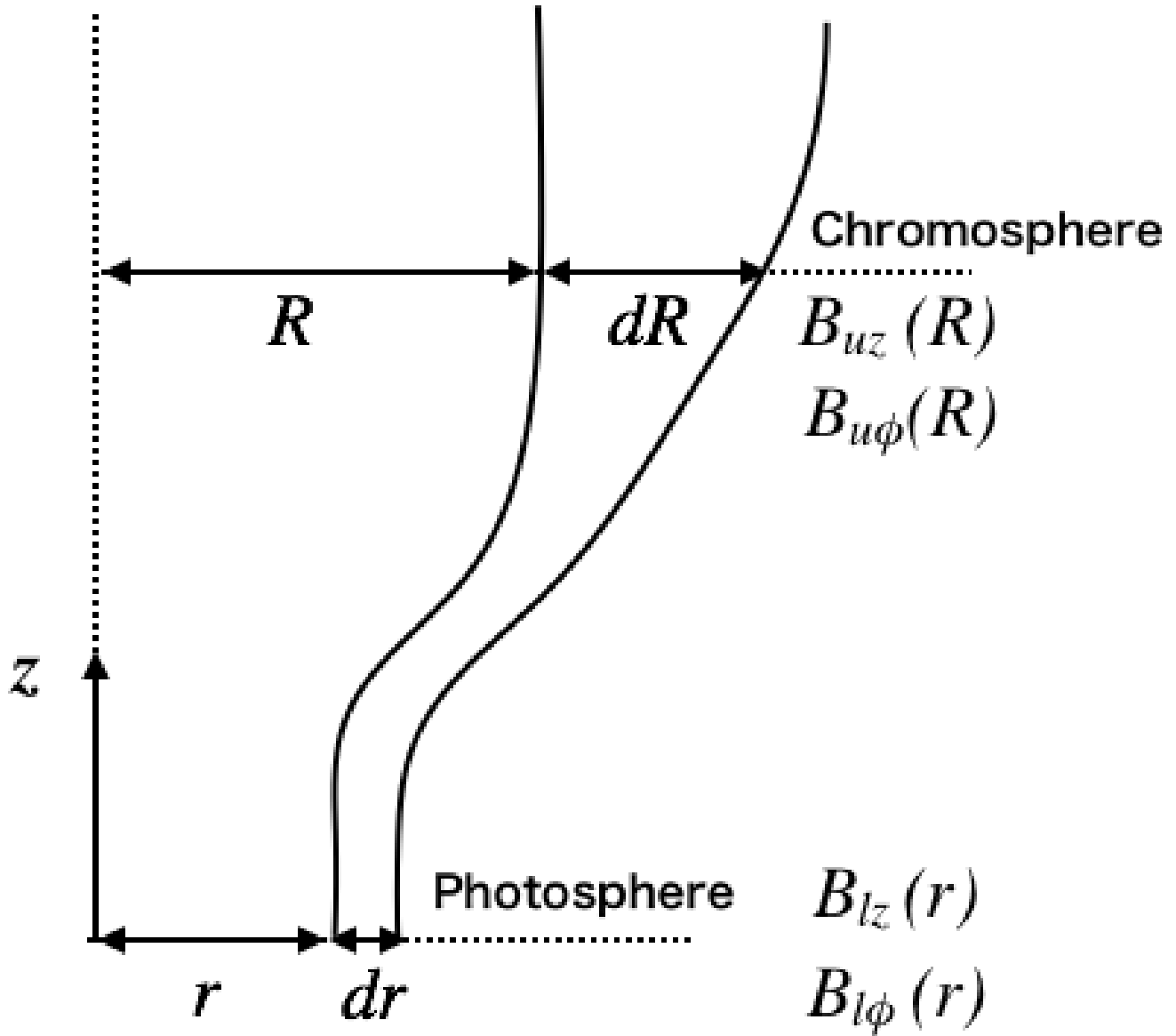


**Figure 16.** Sketch of the expansion of the magnetic flux tube. Solid lines show the magnetic field lines.

expansion of the flux tube enhances the non-potentiality at chromospheric heights and suggests that the gas pressure significantly affects the magnetic field even in active regions. Since NLFFF calculation is based on the photospheric magnetic field in this study, the effect of expansion of the magnetic flux tubes can not be reproduced. The underestimation can be found even in NOAA 11861, which satisfies force-free condition evaluated with Equations (4), (5), and (6). We have to note that the force-free conditions in Equations (4), (5), and (6) are not sufficient conditions but necessary conditions. Our results imply that even though

the the force-free conditions in Equations (4), (5), and (6) are satisfied, the effect of force-freeness in the photosphere can be found in the upper atmosphere.

The second possible cause is the uncertainty in the magnetic field observations of the photospheric layer in the penumbral regions. [Lites et al. \(2002\)](#) reported that the magnetic field in the penumbral region has fluted structure. In other words, the penumbra may have two magnetic field components in one pixel. We inverted the photospheric lines Fe I 6301.5 Å and 6302.5 Å with only a single Milne-Eddington component. The presence of several components on the same pixel might lead to a biased estimation of the azimuth of the magnetic field in the penumbral regions.

Our NLFFF modeling and its comparison with the inferred magnetic field strongly suggest that the non-potentiality in active regions may be larger than that previously estimated based on the NLFFF extrapolation not only in the chromosphere but also in the corona. A quantitative estimation of the non-potentiality in the upper atmosphere is important in understanding the onset mechanism for solar flares. Magneto-hydrodynamical instabilities are considered to be important mechanisms for the onset of the eruption of magnetic flux rope and are sensitive to the 3D magnetic field structure. As one of such instabilities, the kink instability ([Török et al. 2004](#)) occurs when the twist of the magnetic flux rope exceeds a critical value, so that it can be characterized by the twist number  $T_w$  ([Berger & Prior 2006](#)) of the flux rope,

$$T_w = \frac{1}{4\pi} \int \alpha dl, \quad (18)$$

where  $l$  is the length along the magnetic field line and  $\alpha$  is the force-free parameter. [Jing et al. \(2018\)](#) performed a statistical study of the relation among the CME occurrence and the presence of MHD instabilities (torus and kink instabilities) based on NLFFF extrapolation. Their conclusion is that kink instabilities play little role in discriminating between confined and ejective events.

Our results show that the magnitude of the underestimation of the non-potentiality is different from each other in the two active regions, as shown in Figures 6 and 9. In the linear force free case (LFF), it is relatively easy to compute the twist number as a function of the SSA. To this end, the magnetic field in the LFF case

is given by:

$$\mathbf{B} = \begin{pmatrix} B_x \\ B_y \\ B_z \end{pmatrix} = B_0 \begin{pmatrix} \alpha_0 k^{-1} \cos ky \\ -lk^{-1} \cos ky \\ \sin ky \end{pmatrix} \exp(-lz), \quad (19)$$

where  $\alpha_0$  is the constant force-free parameter,  $k$  is the wave number,  $l = (k^2 - \alpha_0^2)^{1/2}$ , and  $B_0$  is a constant. As usual, when  $\alpha_0 = 0$ , the magnetic field becomes potential field and points along the  $y$ -axis. In this case, the SSA can be calculated as

$$\text{SSA} = \tan^{-1}(-B_x/B_y), \quad (20)$$

$$= \tan^{-1}(\alpha_0/l), \quad (21)$$

so that

$$\alpha_0 = \pm k \sin(\text{SSA}). \quad (22)$$

Because  $\alpha_0$  is constant along the field line, the twist number is given by

$$T_w \sim \frac{1}{4\pi} \alpha L = \pm \frac{kL}{4\pi} \sin(\text{SSA}), \quad (23)$$

where  $L$  is the length of the field line. Therefore, when the SSA increases from  $10^\circ$  to  $40^\circ$ , the twist number increases by a factor 3.7. Likewise, when the SSA increases from  $30^\circ$  to  $50^\circ$ , the twist number only increases by a factor 1.5. If this behavior is approximately maintained in the NLFFF case, we find an underestimation of a factor  $\sim 2$  of the twist number for NOAA 11158, which goes up to more than 3 for the case of NOAA 10969. This will significantly affect the probability of the occurrence of ejective flares in these regions.

Although our results reveal the incompleteness in the current NLFFF modelings, we do not conclude that the extrapolation method is unnecessary. There are several points to discuss the topic. Firstly, our results are based on the analysis of two active regions. It is too early to conclude that the extrapolation method is not reliable. Further investigations with statistical analysis are required. Secondly, the main cause of the failure has a possibility to be solved. We attribute the failure of the current NLFFF modeling to the non-force-freeness (high plasma-beta) in the photosphere. The plasma beta decreases as the height increases

and is thought to be sufficiently small at the chromospheric height (Gary 2001). Therefore, the inclusion of chromospheric magnetic field to the NLFFF modeling could improve the NLFFF modeling. Thirdly, the reliable extrapolation results in the solar corona are not guaranteed even if we use the chromospheric magnetic field as another constraint. The extrapolation methods have other problems to be solved in addition to the non-force-freeness in the photosphere. The results of the NLFFF extrapolation have the dependency on the method (DeRosa et al. 2009), spatial resolution (DeRosa et al. 2015), and initial guess (Kawabata et al. 2020). More efforts should be made to solve such problems and develop more reliable extrapolation method. Fourthly, the coronal magnetic fields are expected to be measured by the Daniel K. Inouye Solar Telescope (DKIST: Keil et al. 2011). Although DKIST will provide fascinating data of the coronal magnetic field, we think that the extrapolation method is still necessary. The extrapolation method and the direct coronal magnetic field measurements are complementary. While the coronal measurements of DKIST is limited to the limb, the extrapolation methods are usually applied to on-disk observations. Utilizing both information of the extrapolation and direct measurements is important to tackle the questions of the solar corona.

## 6. SUMMARY

We examined the chromospheric magnetic fields from spectropolarimetric observations of the He I 10830 Å multiplet, which were compared with the chromospheric magnetic field extrapolated from the photospheric magnetic field. Our main conclusions are:

- (1): The chromospheric magnetic field derived from the spectropolarimetric observations shows more twisted magnetic fields at several locations than the photospheric magnetic field does.
- (2): The potential field and NLFFF extrapolation from the photospheric magnetic field underestimate the non-potentiality at the chromospheric height at many locations.

From the analysis for two active regions, we have revealed that the magnetic field in the upper atmosphere may have higher non-potentiality than previously thought based on the NLFFF modeling. Our studies emphasize the importance of the chromospheric magnetic field measurements for more accurate 3D magnetic field modeling and the understanding of the non-potentiality in active region corona. Because the

non-potentiality is a crucial ingredient in investigating the MHD instability, our findings are important for understanding the onset mechanisms for solar flares and CMEs, which affect the environment in the solar system. In the current state, the chromospheric magnetic field observations in active regions are very few in number. It is obvious that we should make efforts to perform more observations of the chromospheric magnetic fields in flare-productive active regions with future large aperture telescopes.

**Acknowledgements** The authors thank to the referee for useful comments. *Hinode* is a Japanese mission developed and launched by ISAS/JAXA, collaborating with NAOJ as a domestic partner, NASA and STFC (UK) as international partners. It is operated by these agencies in cooperation with ESA and NSC (Norway). We gratefully acknowledge the *SDO/HMI* team for providing data. Our calculations of NLFFF modeling were performed on JAXA Supercomputer System generation 2 (JSS2). This publication makes use of data obtained during Cycle 2 DST Service Mode Operations under the proposal ID P495. This work was supported by MEXT/JSPS KAKENHI Grant Numbers JP15H05814 and JP18H05234. AAR acknowledges financial support from the Spanish Ministerio de Ciencia, Innovación y Universidades through project PGC2018-102108-B-I00 and FEDER funds.

## REFERENCES

- Aschwanden, M., De Pontieu, B., & Katrukha, E. 2013, *Entropy*, 15, 3007
- Asensio Ramos, A., de la Cruz Rodríguez, J., Martínez González, M. J., & Socas-Navarro, H. 2017, *A&A*, 599, A133
- Asensio Ramos, A., Trujillo Bueno, J., & Landi Degl'Innocenti, E. 2008, *ApJ*, 683, 542
- Bamba, Y., Kusano, K., Yamamoto, T. T., & Okamoto, T. J. 2013, *ApJ*, 778, 48
- Beck, C., Schmidt, W., Kentischer, T., & Elmore, D. 2005, *A&A*, 437, 1159
- Berger, M. A., & Prior, C. 2006, *Journal of Physics A Mathematical General*, 39, 8321
- Bobra, M. G., Sun, X., Hoeksema, J. T., Turmon, M., Liu, Y., Hayashi, K., Barnes, G., & Leka, K. D. 2014, *SoPh*, 289, 3549
- Casini, R., Judge, P. G., & Schad, T. A. 2012, *ApJ*, 756, 194
- Collados, M., Lagg, A., Díaz Garcí A, J. J., Hernández Suárez, E., López López, R., Páez Mañá, E., & Solanki, S. K. 2007, in *Astronomical Society of the Pacific Conference Series*, Vol. 368, *The Physics of Chromospheric Plasmas*, ed. P. Heinzel, I. Dorotovič, & R. J. Rutten, Heinzel

- Collados, M., Rodríguez Hidalgo, I., Bellot Rubio, L., Ruiz Cobo, B., & Soltau, D. 1999, in *Astronomische Gesellschaft Abstract Series*, Vol. 15, *Astronomische Gesellschaft Abstract Series*, ed. R. E. Schielicke, 11
- Collados, M. V. 2003, in *Proc. SPIE*, Vol. 4843, *Polarimetry in Astronomy*, ed. S. Fineschi, 55–65
- de la Cruz Rodríguez, J., & Socas-Navarro, H. 2011, *A&A*, 527, L8
- de la Cruz Rodríguez, J., & van Noort, M. 2017, *SSRv*, 210, 109
- Dedner, A., Kemm, F., Kröner, D., Munz, C.-D., Schnitzer, T., & Wesenberg, M. 2002, *Journal of Computational Physics*, 175, 645
- Delbouille, L., Roland, G., Brault, J. W., & Testerman, L. 1981
- DeRosa, M. L., et al. 2009, *ApJ*, 696, 1780
- . 2015, *ApJ*, 811, 107
- Gary, G. A. 2001, *SoPh*, 203, 71
- Handy, B. N., et al. 1999, *SoPh*, 187, 229
- Ichimoto, K., et al. 2008, *SoPh*, 249, 233
- Inoue, S., Magara, T., Pandey, V. S., Shiota, D., Kusano, K., Choe, G. S., & Kim, K. S. 2014, *ApJ*, 780, 101
- Jaeggli, S. A., Lin, H., Mickey, D. L., Kuhn, J. R., Hegwer, S. L., Rimmele, T. R., & Penn, M. J. 2010, *MmSAI*, 81, 763
- Jing, J., Liu, C., Lee, J., Ji, H., Liu, N., Xu, Y., & Wang, H. 2018, *ApJ*, 864, 138
- Joshi, J., Lagg, A., Hirzberger, J., & Solanki, S. K. 2017, *A&A*, 604, A98
- Kawabata, Y., Inoue, S., & Shimizu, T. 2020, arXiv e-prints, arXiv:2005.00177
- Keil, S. L., Rimmele, T. R., Wagner, J., Elmore, D., & ATST Team. 2011, in *Astronomical Society of the Pacific Conference Series*, Vol. 437, *Solar Polarization 6*, ed. J. R. Kuhn, D. M. Harrington, H. Lin, S. V. Berdyugina, J. Trujillo-Bueno, S. L. Keil, & T. Rimmele, 319
- Kosugi, T., et al. 2007, *SoPh*, 243, 3
- Kusano, K., Bamba, Y., Yamamoto, T. T., Iida, Y., Toriumi, S., & Asai, A. 2012, *ApJ*, 760, 31
- Lagg, A., Woch, J., Krupp, N., & Solanki, S. K. 2004, *A&A*, 414, 1109
- Landi Degl’Innocenti, E., & Landolfi, M., eds. 2004, *Astrophysics and Space Science Library*, Vol. 307, *Polarization in Spectral Lines*
- Leka, K. D., Barnes, G., & Crouch, A. 2009, in *Astronomical Society of the Pacific Conference Series*, Vol. 415, *The Second Hinode Science Meeting: Beyond Discovery-Toward Understanding*, ed. B. Lites, M. Cheung, T. Magara, J. Mariska, & K. Reeves, 365
- Lemen, J. R., et al. 2012, *SoPh*, 275, 17
- Lites, B. W., & Ichimoto, K. 2013, *SoPh*, 283, 601
- Lites, B. W., Socas-Navarro, H., Skumanich, A., & Shimizu, T. 2002, *ApJ*, 575, 1131
- Lites, B. W., et al. 2013, *SoPh*, 283, 579
- Liu, S., Su, J. T., Zhang, H. Q., Deng, Y. Y., Gao, Y., Yang, X., & Mao, X. J. 2013, *PASA*, 30, e005
- Low, B. C. 1985, in *Measurements of Solar Vector Magnetic Fields*, ed. M. J. Hagyard
- Martínez-Sykora, J., De Pontieu, B., Carlsson, M., & Hansteen, V. 2016, *ApJL*, 831, L1

- Merenda, L., Lagg, A., & Solanki, S. K. 2011, *A&A*, 532, A63
- Metcalf, T. R. 1994, *SoPh*, 155, 235
- Metcalf, T. R., Jiao, L., McClymont, A. N., Canfield, R. C., & Uitenbroek, H. 1995, *ApJ*, 439, 474
- Moon, Y.-J., Choe, G. S., Yun, H. S., Park, Y. D., & Mickey, D. L. 2002, *ApJ*, 568, 422
- Parker, E. N. 1974, *ApJ*, 191, 245
- Schad, T. A., Penn, M. J., & Lin, H. 2013, *ApJ*, 768, 111
- Schad, T. A., Penn, M. J., Lin, H., & Tritschler, A. 2015, *SoPh*, 290, 1607
- Shimizu, T., et al. 2008, *SoPh*, 249, 221
- Socas-Navarro, H. 2001, in *Astronomical Society of the Pacific Conference Series*, Vol. 236, *Advanced Solar Polarimetry – Theory, Observation, and Instrumentation*, ed. M. Sigwarth, 487
- Solanki, S. K., Lagg, A., Woch, J., Krupp, N., & Collados, M. 2003, *Nature*, 425, 692
- Suematsu, Y., et al. 2008, *SoPh*, 249, 197
- Török, T., Kliem, B., & Titov, V. S. 2004, *A&A*, 413, L27
- Trujillo Bueno, J. 2001, in *Astronomical Society of the Pacific Conference Series*, Vol. 236, *Advanced Solar Polarimetry – Theory, Observation, and Instrumentation*, ed. M. Sigwarth, 161
- Tsuneta, S., et al. 2008, *SoPh*, 249, 167
- Vernazza, J. E., Avrett, E. H., & Loeser, R. 1981, *ApJS*, 45, 635
- Wang, H., et al. 2017, *Nature Astronomy*, 1, 0085
- Wiegelmann, T., Inhester, B., & Sakurai, T. 2006, *SoPh*, 233, 215
- Wiegelmann, T., & Sakurai, T. 2012, *Living Reviews in Solar Physics*, 9, 5
- Xu, Z., Lagg, A., Solanki, S., & Liu, Y. 2012, *ApJ*, 749, 138
- Yamamoto, T. T., & Kusano, K. 2012, *ApJ*, 752, 126
- Yelles Chaouche, L., Kuckein, C., Martínez Pillet, V., & Moreno-Insertis, F. 2012, *ApJ*, 748, 23